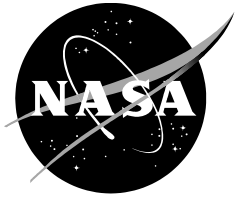# Documentation of the Recirculation in a Closed-Chamber Rotor Hover Test

Miranda McCoy
Defense Nuclear Facilities Safety Board
Washington, DC 20004

Alan J. Wadcock
Larry A. Young
Ames Research Center
Moffett Field, California 94035

August 2016

NASA STI Program ... in Profile

Since its founding, NASA has been dedicated to the advancement of aeronautics and space science. The NASA scientific and technical information (STI) program plays a key part in helping NASA maintain this important role.

The NASA STI program operates under the auspices of the Agency Chief Information Officer. It collects, organizes, provides for archiving, and disseminates NASA's STI. The NASA STI program provides access to the NTRS Registered and its public interface, the NASA Technical Reports Server, thus providing one of the largest collections of aeronautical and space science STI in the world. Results are published in both non-NASA channels and by NASA in the NASA STI Report Series, which includes the following report types:

- TECHNICAL PUBLICATION. Reports of completed research or a major significant phase of research that present the results of NASA Programs and include extensive data or theoretical analysis. Includes compilations of significant scientific and technical data and information deemed to be of continuing reference value. NASA counterpart of peer-reviewed formal professional papers but has less stringent limitations on manuscript length and extent of graphic presentations.

- TECHNICAL MEMORANDUM. Scientific and technical findings that are preliminary or of specialized interest, e.g., quick release reports, working papers, and bibliographies that contain minimal annotation. Does not contain extensive analysis.

- CONTRACTOR REPORT. Scientific and technical findings by NASA-sponsored contractors and grantees.

- CONFERENCE PUBLICATION. Collected papers from scientific and technical conferences, symposia, seminars, or other meetings sponsored or co-sponsored by NASA.

- SPECIAL PUBLICATION. Scientific, technical, or historical information from NASA programs, projects, and missions, often concerned with subjects having substantial public interest.

- TECHNICAL TRANSLATION. English-language translations of foreign scientific and technical material pertinent to NASA's mission.

Specialized services also include organizing and publishing research results, distributing specialized research announcements and feeds, providing information desk and personal search support, and enabling data exchange services.

For more information about the NASA STI program, see the following:

- Access the NASA STI program home page at http://www.sti.nasa.gov

- E-mail your question to help@sti.nasa.gov

- Phone the NASA STI Information Desk at 757-864-9658

- Write to:
  NASA STI Information Desk
  Mail Stop 148
  NASA Langley Research Center
  Hampton, VA 23681-2199
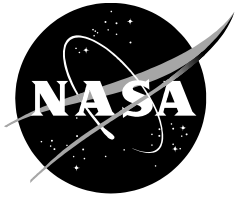
Documentation of the Recirculation in a Closed-Chamber Rotor Hover Test

Miranda McCoy
Defense Nuclear Facilities Safety Board
Washington, DC 20004

Alan J. Wadcock
Larry A. Young
Ames Research Center
Moffett Field, California 94035

National Aeronautics and
Space Administration

Ames Research Center
Moffett Field, CA 94035-1000

August 2016

Acknowledgments

Special thanks must go to the entire WT-1 crew including, but not limited to, Geoffrey Ament, Eduardo Solis, Alexis Twine, and Michelle Dominguez; controls expert Farid Haddad; the Ames Research Center Machine Shop; everyone at JPL who woke up early, stayed late, and did everything possible to facilitate this test, and finally to Ames Research Center Code AV Branch Chief William Warmbrodt for his continual interest and motivation.

Table of Contents

Table of Contents (cont.)

List of Figures

List of Tables

Nomenclature

A	rotor plan-form area, $\pi D^2 / 4$
C	speed of sound
C_T	rotor thrust coefficient, $T / (\rho V_{tip}^2 A)$
D	rotor diameter
r, Θ, Z	orthogonal directions in rotor coordinates
R	rotor radius
T	rotor thrust
V	velocity
V_{tip}	rotor blade tip speed, ΩR
X, Y, Z	orthogonal directions in probe coordinates
ρ	air density
Ω	rotor RPM
σ	RMS velocity fluctuation
ARMD	Aeronautics Research Mission Directorate
CF	Compact Flash
CMOS	Complementary Metal-Oxide-Semiconductor
HID	High-Intensity Discharge
JPL	Jet Propulsion Laboratory
LCD	Liquid Crystal Display
LSB	Least Significant Bit
MRTS	Mars Rotor Test Stand
MSH	Mars Scout Helicopter
NASA	National Aeronautics and Space Administration
NFAC	National Full-Scale Aerodynamics Complex
PAD	Personnel Access Door
PST	Pacific Standard Time
RC	Radio Controlled
RCC	Rotor Control Console

Nomenclature (cont.)

RMS	Root Mean Square
RotCFD	Rotor Computational Fluid Dynamics, an unsteady Navier–Stokes solver optimized for rotary wings
RPM	Revolutions Per Minute
SLR	Single Lens Reflex
USB	Universal Serial Bus
UV	Ultraviolet
VAC	Voltage Alternate Current
VDC	Voltage Direct Current
WT-1	Weather Test 1

Documentation of the Recirculation in a Closed-Chamber Rotor Hover Test

Miranda McCoy,[1] Alan J. Wadcock,[2] and Larry A. Young[2]

Summary

A rotor hover test was performed inside the JPL 25-foot-diameter Space Simulator. The 40-inch-diameter rotor was tested at two locations in the chamber—on the chamber centerline and 2m off-axis. The rotor was tested in both upright and inverted configurations for $500 < RPM < 2000$. Fluorescent tufts were used to identify regions of recirculation. Velocities on the entrainment side of the rotor were measured. Tabulated values for the mean entrainment velocity components and the corresponding root mean square velocity fluctuations are provided. Unsteady velocity measurements provide a description of the turbulence ingested into the rotor plane and quantify the unsteady velocity field that the Mars Scout Helicopter can expect to encounter during free flight inside the Space Simulator.

Introduction

In July 2014, as part of the NASA Mars Exploration program (a long-term effort of robotic exploration of the red planet) NASA announced a new robotic science rover with a planned launch in 2020 (ref. 1). The 2020 Mars rover will be the size of a small car—about 10 feet long, 9 feet wide, and 7 feet tall—and will carry seven carefully selected science instruments.

This report describes part of the broader effort to design and test a helicopter capable of working in tandem with the Mars rovers to explore the surface of Mars. While the Mars rovers are necessarily limited in their capacity for exploration by distance and topography, a Mars helicopter would be able to traverse difficult terrain quickly. This helicopter could provide input for planning efficient rover paths and, moreover, visit some of the interesting rover-inaccessible features of the Martian landscape such as the layered cliff faces along the walls of Valles Marineris or the headwaters of the Martian gullies. A vehicle of this type would be capable of acquiring small samples, providing limited in-situ surveys, and surveying the geography remotely. Experimental testing toward this goal began in the early 2000s with isolated rotor testing in the NASA Ames Planetary Aeolian Laboratory (refs. 2,3). This testing was performed in a low-density atmosphere close to that of Mars but without matching temperature or atmospheric composition. Throughout the early- to mid-2000s, research was conducted into developing mission plans, baseline proof-of-concept rotors, coaxial rotor hover testing, flight demonstrations, and scoping of vehicle parameters. Unfortunately, this research concluded in the mid-2000s, and shifting priorities left the project stagnant until 2014.

With the 2020 Mars Mission on the horizon, the idea of a Mars Scout Helicopter (MSH) was recently revived, efforts being concentrated at the Jet Propulsion Laboratory (JPL) and supported by NASA Ames Research Center. A small group of engineers at JPL are currently working on the design of a small helicopter that can be stored in a furled state beneath the rover during transportation to Mars. Upon landing on Mars, the rover will lower the furled helicopter to the planet surface and drive off, leaving the helicopter to self deploy. The MSH has not yet been accepted as a payload on the 2020 launch. The JPL

[1] Defense Nuclear Facilities Safety Board, Washington, DC 20004
[2] NASA Ames Research Center, Moffett Field, CA 94035

group is, however, hoping to design, build, and test the MSH in time to win approval for inclusion on the 2020 Mars rover launch (ref. 4). The latest official diameter of the MSH rotor is 1.10m. The weight of the MSH is currently limited to 1 kg (including solar array and on-board batteries). The design goal is to provide sufficient power for short helicopter flights up to 60 seconds.

Approximately 1-1/2 to 2 years ago, JPL contacted the Aeronautics Research Mission Directorate (ARMD) to pursue the possibility of collaboration on MSH development. In January 2015 JPL was focused on two areas—the deployment of the helicopter from beneath the rover and the possibility of using closed-loop-control of the helicopter. Young, at Ames Research Center (refs. 2,3), had been studying the possibility of a Mars helicopter for some years and recognized the need to consider recirculation effects when measuring hover performance and making system identification measurements in a closed chamber. Therefore, in early 2015, Young started modeling the Mars rotor mounted in the JPL Space Simulator using RotCFD (an Unsteady Navier–Stokes solver optimized for rotary wings, ref. 5).

In April 2015 the JPL MSH team visited Ames Research Center to bring Ames up to speed and to discuss specific areas of collaboration prior to planned JPL rotor testing; JPL anticipated testing the MSH in the JPL 25-foot-diameter Space Simulator between January and June 2016. At this meeting it was determined that it would be highly beneficial for Ames Research Center to perform a hover test in the JPL Space Simulator in order to experimentally confirm recommendations provided to JPL based on earlier RotCFD computations performed by Young. These computations indicated that mounting the rotor upside-down, in a "thrust-down, wake-up" configuration, would be optimal for simulating "free-air" rotor hover performance as this configuration avoids recirculation close to the rotor plane. In addition, RotCFD computations were being used to provide estimates for the turbulence entrained into the rotor plane—the so-called "weather" inside the Space Simulator—and these numbers were being used by JPL to determine if the vehicle design had sufficient control authority for forward flight inside the chamber. This test was given the name "Weather Test 1" (WT-1) reflecting the second goal of the test, namely the measurement of turbulence entrained into the rotor plane (and validation of RotCFD "weather" prediction inside the chamber).

For maximum benefit to the JPL endeavor, WT-1 had to be completed before JPL started testing the MSH rotor in the Space Simulator. JPL planned to start model buildup inside the Space Simulator in January, with end of testing expected in June 2016. WT-1 was therefore scheduled for early December 2015. One week of chamber occupancy was approved to allow for model installation, testing, and removal. One chamber pump-down to Mars-representative atmospheric density levels was also authorized, if needed.

Objectives

The objectives of WT-1 were to confirm RotCFD computations for hover testing inside the Space Simulator, namely:

a) With rotor test stand on centerline of Space Simulator:

   1) Demonstrate that testing the rotor in conventional (upright) orientation (thrust = up, wake = down) results in strong recirculation beneath the rotor plane.

   2) Demonstrate that testing the rotor in inverted orientation (thrust = down, wake = up) eliminates the recirculation beneath the rotor plane.

   3) Measure the three-component velocity field being entrained into the rotor plane for both upright and inverted rotors at selected distances from the rotor disk for comparison with entrained turbulence predicted by RotCFD.

b) With rotor test stand located 2m off-axis inside Space Simulator:

   1) Measure inflow velocities into the rotor plane for upright rotors only (thrust = up, wake = down), at selected distances above the rotor disk, for comparison with RotCFD predictions. These off-axis measurements of inflow are needed to determine the off-axis entrained turbulence level and provide guidance on the level of control authority needed for flight test of the JPL MSH inside the Space Simulator under Mars-representative atmospheric densities.

Test Plan

JPL informed the Ames Research Center team that the MSH rotors and test stand would not be available for testing during WT-1, as design and construction were incomplete. This necessitated finding an acceptable test stand and rotor in short order. The Mars Rotor Test Stand (MRTS) used by Young (refs. 2,3) had been mothballed some time ago and was brought out of storage along with the rotor control console. An acceptable location was rapidly identified for complete operational checkout of the test stand in excess of 2000 RPM.

Simultaneously, measurements were being planned and designed to visualize the anticipated flow recirculation beneath the rotor (in conventional upright installation) and make entrainment velocity measurements (three-component) at selected points in the *inflow* velocity field to validate RotCFD "weather forecast" predictions inside the chamber. These measurements would be performed for two MRTS locations in the chamber. First, on the chamber centerline for validation of RotCFD predictions in hover, and second, displaced 2m towards the chamber wall to document variations in inflow (turbulence) as a function of radial location inside the chamber for follow-on free flight testing of the MSH inside the Space Simulator by JPL.

It was assumed that an adequate simulation of the recirculation caused by MSH hover in the Space Simulator could be achieved by matching rotor diameter and V_h (the hover-induced velocity through the rotor disk). An acceptable simulation of the four-bladed coaxial contra-rotating MSH rotor would be a 40-inch-diameter pair of coaxial, co-rotating, fixed-pitch propeller blades mounted at 90 degrees to each other. Both JPL and Ames were confident that adequate hover performance measurements could be achieved without the requirement to evacuate the chamber to Mars-representative densities, although this option remained in the test plan, and one chamber pump-down had been approved. By sweeping RPM, some idea of the significance of Reynolds Number could be deduced.

Young recommended that the MSH rotor be tested with the rotor hub 10 feet above the floor of the chamber to mount the rotor out of ground effect and to invert the rotor (thrust = down, wake = up) to minimize the effect of recirculation inside the chamber. The plan was to document flow recirculation beneath the rotor disk using fluorescent micro-tufts. Micro-tufts were selected because of their performance in low velocity environments at both Earth's and Mars' atmospheric densities (albeit with Earth's gravity). The recirculation flow pattern indicated by tufts was to be compared with RotCFD calculations. Inflow velocities into the rotor disc were planned using a sonic anemometer placed at a few selected locations on the entrainment side of the rotor disk for both the upright and inverted geometries. Measurements of turbulence ingested into the rotor disk would also be compared with RotCFD calculations. The latter information was expected to be useful in determining if the MSH had sufficient control authority to maintain steady flight inside the JPL chamber during free flight testing. Turbulence measurements at representative Mars' atmospheric densities were desirable but not essential.

This report describes essential details of the WT-1 "Weather Test." No comparison of measurements with RotCFD calculations is provided in this report.

Facility Description

WT-1 took place in the JPL 25-foot-diameter Space Simulator shown in Figure 1. This facility was designed for environmental testing of unmanned spacecraft under simulated interplanetary conditions of extreme cold, high vacuum, and intense solar radiation. For the purposes of WT-1 however, the cooling, vacuum, and solar simulation capabilities were not used. All WT-1 testing was performed in the unmodified pressure and temperature of the facility. The Space Simulator is a stainless-steel cylindrical test chamber with an internal diameter of 25 feet and a height of 85 feet. The walls and floor are lined with aluminum shrouds and fins for cooling the chamber for cryogenic tests.

The 25-foot-wide access door was initially opened to permit the original MRTS installation on the chamber centerline. It was also opened to gain access to the rotor hub in order to change the direction of rotor thrust. This was a model change that required personnel to be inside the chamber for up to 2 hours in order to disassemble the hub assembly, and carbon dioxide buildup was a safety concern. It was felt that the Personnel Access Door (PAD) in the center of the 25-foot-wide access door provided insufficient air exchange for personnel spending extended time inside the chamber.

To relocate the MRTS 2m off-axis later in the test, the 25-foot-wide access door was opened in order to use the crane. During the test, the PAD was the preferred method of entry to the chamber either to reposition the sonic anemometer or to free tangled tufts.

Mars Rotor Test Stand Description

The swash plate and collective pitch controls were removed from the original MRTS described in references 2 and 3. A new adapter plate was designed to interface with the new rotor blades. The original MRTS drive motor and Rotor Control Console (RCC) were retained.

Mars Rotor Test Stand and Blast Shield

The MRTS consists of a cylindrical column bolted to a 4-foot-square baseplate, motor, drive assembly, and RPM sensor as shown in Figure 2. The test stand is 12.75 inches in diameter, which is significant compared to the rotor diameter of 40 inches. The MRTS has a Siemens Electric AC Feed Drive Motor (model #1FT5104-0AF71-1) with a DC Link voltage of 600 and a maximum RPM of 3000. The highest motor speed during system checkout at Ames Research Center was 2500 RPM.

Concern over the possibility of rotor failure at high RPM led to a last minute decision to provide blast shield protection to limit possible damage to the JPL Space Simulator. It was acknowledged that any blast shield would compromise the attempt to measure rotor hover performance, but the effect on the induced flow into the rotor should be minimal, implying that the planned inflow velocity measurements should remain meaningful. RotCFD was used to examine multiple blast shield geometries—round, square, and octagonal—and to compare them with the "no-shield" case. The square blast shield was chosen because the calculated Figure of Merit was closest to that for the no-shield case for both upright and inverted rotor testing.

4

Figure 3 shows a sketch of the blast shield surrounding the rotor and hub. In order to minimize flow interference the blast shield is limited to a vertical extent of 2 feet. The blast shield is 0.25 inches thick, made from A36 structural steel plate (yield strength 36,000 psi), and designed to resist fragmentation at 3000 RPM. The blast shield is supported on four steel L-beams, each leg bolted to the top of a square steel box beam, which, in turn, is bolted to the 4-foot-square steel baseplate.

Apart from the blast shield, this is the same assembly used in the original Ames Planetary Aeolian Laboratory isolated rotor testing in the early 2000s. Power to the MRTS is controlled via a switch on the RCC. Rotor RPM is controlled by a potentiometer on the RCC and displayed on the RCC via a digital panel meter. A switch on the RCC selects the direction of hub rotation.

Three load cells were available for measuring rotor thrust and were used during system checkout at Ames Research Center. To prevent damage, load cells were removed for the journey to JPL. During system checkout at JPL, increased vibration levels were encountered compared to those observed at Ames. The measurement of rotor thrust was deemed noncritical for WT-1 testing, so the load cells were not installed in order to avoid their possible damage.

Rotor and Rotor Hub

The rotor blades used in WT-1 are commercial off-the-shelf RC super-class propeller blades manufactured by Biela Propeller Company and purchased from Troy Built Models. Propellers come pre-balanced and approved for operation up to 6000 RPM. They are handmade using carbon fiber and epoxy. The blades are hollow and the tips are solid. The hub of the propeller is made from hardwood and comes equipped with a central mounting hole. The propellers are supplied with a hard, durable, gel coat finish; they are light but very stiff.

The 40-inch-diameter propellers chosen for the current study are each two-bladed as shown in Figure 4. They are mounted in a stacked configuration with a fixed angle of 90 degrees relative to each other. Figure 5 shows a photograph of the assembly. Each propeller hub is 1.77 inches thick, and the spacer between the two propellers is 0.80 inches thick. This defines the rotor spacing to be 2.57 inches.

The model number for the propeller, 40 x 22, is clearly visible in Figure 5. The two propellers spin in unison and are both fixed via a custom steel hub to a single motor shaft at the top of the MRTS. The custom hub was modified from the original Ames Planetary Aeolian Laboratory isolated-rotor-test hub, reworked to interface with the new rotor.

During "thrust-up" operation the rotor spins counterclockwise when viewed from above, and during "thrust-down" operation the rotor spins in the opposite direction.

Accelerometers

Two accelerometers mounted 90 degrees apart in the horizontal plane were installed at the top of the test stand to document stand vibration. These accelerometers were uniaxial 5g Kistler accelerometers. They were rigidly mounted directly to the test stand with epoxy. Maximum rated RPM for the motor is 3000. This corresponds to a shaft 1/rev frequency of 50 Hz. Accelerometer signals were sampled at 200 Hz, and displayed and stored on an Astro-Med Dash 18X data acquisition system. The accelerometers were the sole safety-of-flight instrumentation. The real-time accelerometer signals were continuously monitored on the Astro-Med virtual strip-chart recorder. The accelerometer signals were not anti-alias filtered, as vibrational spectra were not required. Peak-to-peak accelerometer readings were observed on the Astro-Med and monitored for amplitude growth throughout the test.

Data Acquisition

Data collected during WT-1 included tuft grid images, sonic anemometer three-component velocity time history measurements, and accelerometer data. For all data points, sonic anemometer and accelerometer measurements were acquired. Tuft photographs were acquired for all runs except Run2 (due to a malfunction).

An Astro-Med Dash 18X data acquisition system was used for both data collection and real-time monitoring of analog anemometer and accelerometer signals. The Dash 18X is a 14-bit data acquisition and real-time monitoring system that allows for sensor calibration input and filter application. All Astro-Med data files for the current test are exactly 3 minutes long.

The *digital* output stream from the sonic anemometer was also monitored and recorded on a separate laptop with custom CSAT3 software via an RS-232 connection. The standard RS-232 cable supplied with the anemometer is only 25 feet long, insufficient to reach outside the chamber. The existing cable was therefore extended by means of a Gefen Inc. RS232 Extender (model EXT-RS232) and an additional 50-foot CAT-5e Ethernet cable, thereby allowing control over the CSAT3 sonic anemometer from a laptop located outside the chamber. Digital velocity measurements were started and stopped manually. Both analog and digital velocity measurements were designed to acquire data in the quiescent period before rotor spin-up, during rotor spin-up, and for an additional 2 minutes once the rotor reached the desired RPM. The CSAT3 software allows for real-time monitoring as well as data logging. The digital output stream has far superior velocity resolution than the analog out signal. The analog velocity measurement was therefore used as a backup for the digital measurements.

Power cables were kept separate from sensor cables to limit electrical noise in the data. 600 VDC power was routed to the MRTS test stand from the RCC outside the Space Simulator through one of the bulkhead access ports in the chamber sidewall. The same access port was used to route 110 VAC power to the continuous UV light sources. All signal cables (analog velocity, accelerometers, RS232 digital velocity, and USB camera) were routed from the chamber via a separate access port.

Instrumentation

A sonic anemometer was used to document entrainment velocities into the rotor disk. There was no guarantee that the sonic anemometer would function correctly at extremely low pressures, but there was confidence that the probe could acquire accurate three-component measurements of the recirculation inside the chamber at 1 atmosphere in air, which was deemed sufficient.

Sonic Anemometer

Wind speed and direction were measured using a Campbell Scientific CSAT3 3-D Sonic Anemometer shown in Figure 6. The CSAT3 measures wind speed and speed of sound along the three non-orthogonal sonic axes. The wind speeds are then transformed into orthogonal wind components U_x, U_y, and U_z referenced to the anemometer head. Positive y-direction is out of the page. Note the size of the probe volume. The velocity measurement is not a point measurement. The probe coordinate system reflects the orientation normally used for mounting the probe outdoors as a wind speed indicator. For this application, the probe was rotated through 90 degrees in order to place the probe closer to the rotor plane. The side view of the anemometer head shown in Figure 6 becomes the plan view when the probe is rotated through 90 degrees for installation in the chamber. V_x in probe coordinates becomes V_r in rotor coordinates, V_y in probe coordinates becomes V_z in rotor coordinates, and V_z in probe coordinates becomes $-V_\theta$ in rotor

coordinates. In rotor coordinates, Vr is positive radially outwards, V_θ is positive for counterclockwise rotation of the flow when viewed from above, and V_z is positive upwards.

The size of the CSAT3 probe implies that only turbulent scales equal to the probe volume or larger can be measured successfully. Smaller scales enter the probe volume at random locations with random amplitude and phase and are not measurable. The physical size of the CSAT3 probe volume acts as a spatial filter for turbulence measurements. The largest scales are the ones that carry the most turbulent energy, and the CSAT3 successfully measures turbulent scales equal to or larger than the probe volume. The current study is interested in the energy containing turbulent eddies in the recirculating flow, and for this purpose the large probe volume of the sonic anemometer is not a liability.

Both analog and digital anemometer data were acquired at each data point. The anemometer analog output was recorded primarily as backup to the higher resolution digital measurements. Only the digital measurements of velocity are discussed in this report.

The specific CSAT3 sonic anemometer used in the current study had been customized by Campbell Scientific to provide twice the normal operating range for a prior test in the National Full-Scale Aerodynamics Complex (NFAC) 40- by 80-Foot Wind Tunnel. The range and calibration coefficients for this anemometer are therefore not standard. Details of the *custom* CSAT3 probe are provided below:

Analog output:

Voltage range	±5V
Number of bits	12
U_x, U_y, U_z range	±131.072 m/s
LSB	6 cm/s

Digital Output:

Default (standard off-the-shelf CSAT3 probe) digital velocity output (preprogrammed into CSAT32.EXE program) is as follows:

Full-scale wind: ±65.535 m/s, auto-ranging between four ranges; LSB is 0.25 to 2 mm/s.

Speed of sound: 300 to 366 m/s (–50 deg C to +60 deg C); LSB is 1 mm/s.

Because of the customized velocity range of 131.072 m/s for the specific anemometer used in this study, true velocity is TWICE indicated *digital-out* velocity. For the current application, relatively small values of induced velocity towards the rotor plane are expected (as a fraction of full-scale range) implying that the probe always operates in the low velocity mode with the LSB = 0.5 mm/s (twice the default value).

Both analog-out and digital-out velocities indicated by the sonic anemometer were cross-checked against ALNOR handheld anemometer measurements in the velocity field generated by a box fan as a simple sanity check.

Windows PC support software CSAT32.EXE can be used to control and monitor the CSAT3 velocity data in real time and/or collect time series via the RS-232 serial port. The anemometer can be programmed to output four analog signals that correspond to U_x, U_y, U_z, and C. These signals are in the

range of ±5000 mV. The analog output is enabled using the Windows CSAT3 PC support software CSAT32.EXE, and using the CSAT3 RS-232 serial port to connect to the PC RS-232 port.

For the *custom* CSAT3 anemometer:

> Range = 131.072 m/s for U_x, U_y, and U_z.
>
> U_x, U_y, and U_z sensitivity = 26.2144 m/s per volt.
>
> Speed of sound, C = 6.5536 m/s per volt (300 to 366 m/s range).
>
> Note: these are NOT the default calibrations associated with a "standard" off-the-shelf CSAT3 (65.536 m/s velocity range) probe.

The sampling rate for both digital and analog anemometer data was 20 Hz. No filter was applied.

<u>Sonic Anemometer Stand</u>

The sonic anemometer was mounted on a structure composed of 80/20 aluminum extrusions designed to allow quick radial and vertical changes to the position of the anemometer relative to the rotor hub and rotor tip-path-plane as shown in Figure 7. Linear bearings on the vertical beam allow the user to manually raise and lower the anemometer and then lock down the chosen position for the next run. The frame was constructed with a wheeled base for ease of installation in the chamber and adjustment in position once inside the chamber. Wheels are lockable to prevent the structure from moving during the run. Outriggers at the front and back of the stand provide lateral stability, and angled braces on the front and back of the vertical frame provide rigidity fore and aft. The location of the vertical frame can be adjusted between the fore and aft outriggers; one set of braces slides up the vertical frame and the other set of braces slides down the vertical frame to maintain the frame in the vertical plane.

All velocity measurements were made on the inflow side of the rotors at a radial station equal to 75 percent of the blade radius (r = 15 inches) at nominal distances of R and 2R from the topmost rotor. The goal was to measure turbulence in the entrained flow. In order to do this, the anemometer was deliberately kept away from the rotor disk to avoid measurements dominated by blade passage effects.

Fluorescent Micro-Tufts

The challenge of doing flow visualization inside the Space Simulator stems from the reduced density representative of the Mars atmosphere and from the strict requirements imposed on hardware brought into the chamber in order to prevent contamination due to outgassing at low pressure from paints, cables, etc. The simplest, cheapest, and possibly the most attractive approach was determined to be the use of fluorescent micro-tufts to indicate local flow direction. Unfortunately, optical access from outside the chamber is almost nonexistent. It soon became obvious that both the UV light source and camera would have to be inside the chamber. Remote operation was a necessity if testing at reduced density was to occur.

A selection of micro-tuft/mini-tuft materials was available. Smaller diameter tuft materials are expected to respond better in low velocity conditions than the larger diameter materials. As the diameter increases, the tuft rapidly becomes stiff and the "hinge" becomes imperfect. Also, the larger diameter tufts often exhibit "permanent set" reflecting the fact that they were wound on a spool; a larger velocity is required to straighten out the tuft and remove this permanent set. Smaller diameter tufts show complete flexibility, and can fold back on themselves and self-tangle, something that would not happen with the larger

8

diameter tufts. Larger diameter tufts essentially remain straight. Unfortunately the smaller diameter tufts are harder to see.

It makes sense to select the smallest diameter tuft that can be rendered visible with the limited amount of UV light available. Fortunately, the current interest was not to freeze the tuft motion in order to determine the instantaneous flow direction. Long exposure times were desirable in order to determine the average flow direction. Any tuft motion occurring during the image exposure will reveal itself as "tuft coning" providing an estimate for both the average flow direction and the turbulence level at that point.

Tuft Frame

A tuft frame design was needed that would allow the tuft grid to be completely assembled (tufts installed) at Ames and then permit tuft removal prior to shipment of the system to JPL. The tuft frame was designed to cover the complete distance between the MRTS and the chamber wall as closely as possible. Like the sonic anemometer stand, the tuft frame was designed with wheels for ease of maneuverability.

The height of the frame was selected so that the frame could be rolled beneath the bottom of the blast shield allowing flow measurements directly beneath the rotor disk. The tuft frame was constructed from 80/20 aluminum extrusions as shown in Figure 8. The vertical frame was approximately 11 feet long. The top of the frame was designed to be 8 feet above the floor allowing the tuft grid to be rolled underneath the steel blast shield until it approached the rotor test stand. Wheels were lockable to prevent the structure from moving from the desired location during the run. Outriggers at each end of the tuft grid provide lateral stability, and angled guy wires and turnbuckles on either side of the vertical frame provide vertical rigidity. Outriggers were designed to allow the tuft frame to roll over the top of the MRTS baseplate and to butt up against the MRTS if so desired.

Tuft Grid

Black polyester thread was used to construct horizontal supports for the tufts, starting 6 inches below the top aluminum extrusion and thereafter every 12 inches, resulting in seven horizontal thread lines each separated by 1 foot vertically as shown in Figure 9. The thread was appropriately tensioned at either side of the frame. Polyester thread is far superior to cotton thread in terms of tensile strength and was found to be unbreakable at the tension anticipated. Black thread was chosen because it does not fluoresce under UV illumination. Black eyelets were pre-positioned along each horizontal thread at 1-foot increments. The threads were carefully adjusted so that the eyelets were on a 1-foot grid (horizontally and vertically). A single eyelet (size #0, 3/16 inch tall) is shown in Figure 10. The eyelet is one-half of the "hook and eye" closure commonly used as a garment fastener

The current application will not have a meaningful non-zero component of velocity perpendicular to the grid, so tangling of the tufts with any tuft suspension hardware was anticipated. Any tufts that became tangled would need to be untangled before the start of the following run.

Tufts

After extensive testing in the Ames laboratory using the UV source at hand and the camera/lens system available, 0.0007-inch-diameter polyester micro-tufts were selected. The tuft material is supplied as a multifilament thread, and individual 0.0007-inch-diameter strands must be carefully extracted from the multifilament thread. The tuft material is an order of magnitude thinner than a human hair and is essentially invisible in room light.

Calculations were performed to estimate the error in indicated flow direction when testing at 1 atmosphere in air or at 500 Pa in carbon dioxide (in Earth's gravity). The error in the indicated flow direction is easily shown to be independent of tuft length. The maximum error from a 0.0007-inch-diameter polyester tuft used in a carbon dioxide atmosphere at 500 Pa pressure is estimated to be 9 degrees for a typical velocity of 1 m/s when tested in Earth's gravity. The error is less when tested in air at 1 atm.

A short length of tuft material was tied to one end of each black fishing micro-swivel with snap (size 20, length 0.75 inch) shown in Figure 10. The tuft was double-knotted to the swivel to prevent the tuft from coming loose. Room air conditioning was turned off during this process to prevent the tuft from floating away in the slightest breeze. This was a lengthy, extremely tedious procedure. The snap or clasp allows the tuft to be attached to an eyelet on the horizontal thread, or removed at a later time. This was a key part of the design in order to construct the tuft grid at Ames and be able to break it down for shipment to JPL. After all the tufts had been created as described previously, the active length of each tuft was trimmed to 5 inches to preserve the requirement that adjacent tufts not tangle, and the tufts were mounted inside a small book for protection during transportation to JPL.

A total of 77 tufts were needed for the JPL tuft grid (7 rows containing 11 tufts each). Close to 100 tufts were prepared in order to guard against loss during installation (handling of the tufts was considered to be the greatest risk), or loss during testing.

UV Source

Two Electro-Lite Corporation ELC-250 black light lamps provided continuous UV illumination. The ELC-250 is a 250W metal-halide lamp. This is a type of high-intensity discharge (HID) gas lamp. These lamps require a warm-up period of several minutes to reach full light output. The ELC-250 generates long wave UV at 350 nm. The lamp head is separate from the ballast. The lamp head contains the bulb and a reflector designed to control the area of illumination. The front face of the lamp is 5.81 inches (H) x 3.31 inches (V) and is covered with the requisite filter. Testing at Ames indicated good illumination over the full extent of the tuft grid with the UV source 10 to 12 feet ahead of the grid. One UV lamp was proven adequate to render the tufts visible. The second lamp improved the tuft visibility and provided insurance against failure of the first lamp. Each UV lamp and associated ballast was positioned inside the chamber, on the floor of the chamber, directly in front of the tuft grid. During testing, throughout each individual run, both UV lamps were left energized to avoid the warm up needed to achieve full light output after shutdown. The UV lamps were shut down between runs when the sonic anemometer height needed to be changed or the rotor direction of rotation had to be changed. Test section lights were always turned off prior to tuft image acquisition.

Camera

A Nikon D800 digital SLR camera was chosen to record the tuft images. This camera has a 35.9 mm x 24.0 mm CMOS sensor (Nikon FX format) with 36.8 million pixels. Effective image size is 7360 x 4912 pixels (36.1 Mp). A NIKKOR 24-mm F/2 FX lens was chosen to take full advantage of the large sensor size and avoid vignetting. (The camera automatically selects the DX crop mode if a DX lens is attached.) The camera offers standard sensitivities from ISO 100 to 6400, plus enhanced sensitivities up to ISO 25,600 equivalent.

The camera was placed perpendicular to the tuft grid to minimize image distortion, on a tripod that raised the camera height to half the height of the tuft grid. Manual focus was set prior to the first data run and locked in. Using the time-lapse feature on the D800 camera, tuft images were programmed for once every 5 seconds, each with 2-second exposure, with a duration of 100 seconds. This implies a sequence of 21

images. The plan was to commence image acquisition prior to rotor start in order to document the initial quiescent flow, continue through rotor spin-up, and provide documentation of the tuft pattern once the rotor reached the desired RPM. The original plan was to store each image immediately after acquisition on a CF flash card, as this was the fastest way to acquire and store images. With this in mind, a SanDisk 128 GB Extreme Pro CF memory card rated at up to 150 MB/s write speed (tested at 70.5 MB/s average write speed) was purchased and installed in the camera. With this transfer rate, and the planned frame rate of 0.2 Hz, data transfer would not interfere with the planned acquisition sequence.

The software package *ControlMyNikon 5.2* was purchased to provide remote triggering of the camera from outside the chamber—a requirement if testing was performed at reduced pressure inside the chamber. In addition to simple remote triggering of the D800 camera, however, this software provides access to all of the controls normally available via the camera's liquid crystal display (LCD) screen. By choosing to acquire and store images to the laptop instead of the onboard CF card, images were immediately available on the laptop outside the chamber at the end of sequence acquisition. The camera has a USB 3.0 port and was connected to a laptop located outside the chamber via a 50-foot-long USB 3.0 cable with two repeaters. Unfortunately, the laptop only had a USB 2.0 port, so transfer defaulted to the lower rate associated with a USB 2.0. By choosing to save to the laptop instead of the CF card, the image acquisition rate dropped from once every 5 seconds to once every 7 seconds or thereabouts. This was deemed acceptable.

The camera automatically reverts to "live view" after completing the preprogrammed acquisition sequence. Live view of the tuft grid on the laptop allows the acquisition of a test photograph immediately prior to rotor spin-up to verify tufts are free and untangled and flow is quiescent. Then a decision can be made as to when the chamber flow has become stationary after rotor shutdown, and when the next data point can be acquired.

As a result of camera testing performed at Ames, the Nikon D800 with ISO 6400 setting was found to provide the best image quality with negligible noise. The plan for JPL was to run with the lens wide open. Camera placement was supposed to be perpendicular to the tuft frame in order to minimize image distortion and allow image acquisition with minimal depth of field (lens wide open, providing maximum light gathering efficiency). Manual focusing was used and a 21-image sequence was preprogrammed into the camera in order to acquire 1 image every 5 seconds, each with an exposure of 2 seconds. Although testing at Ames had used a single UV light source, two UV light sources were used at JPL to provide maximum UV illumination. The lens was stopped down to F/5.6 to sharpen the tuft image. This may have been due to stray light entering the Space Simulator whereas laboratory testing at Ames had been performed in a darkened room.

Hardware Installation in the Space Simulator

The total weight of the MRTS, including steel baseplate plus blast shield hardware, is estimated to be 2700 pounds. The MRTS is too heavy to be installed directly on the floor of the Space Simulator. Multiple hard points are available inside the Space Simulator for the installation of such heavy test configurations. Figure 11 shows the floor inside the Space Simulator. Five raised hard points, 4 inches above the chamber floor, are evident in the photograph. Two floor panels are absent for repair.

The test called for two rotor test stand locations; first at the center of the chamber and then 2m off-axis. The location of the hard points determines the direction the test stand must be moved to achieve these two positions. A close-up of the JPL hardware provided to interface between the hard points and the MRTS baseplate is shown in Figure 12. Three aluminum I-beams, 5.75 inches tall with 0.25-inch-thick walls, are shown bolted to the tops of the hard points.

Considerable care must be taken to limit chamber contamination due to outgassing of various materials at low vacuum. Before the MRTS could be installed in the Space Simulator, a thorough cleaning was therefore required. The test stand was wiped down with isopropyl alcohol to remove any traces of oil. Access to the interior of the test stand is extremely limited, making it impossible to clean adequately. The test stand was therefore wrapped in Amerstat film held down using Kapton tape. Kapton tape is regularly used as an insulator in ultra-high-vacuum environments because of its low outgassing rate. The blast shield was covered with rust and so received special attention. The motor was cleaned, and all cables were cleaned to remove any oil or dust acquired during system checkout at Ames. Figure 13 shows the MRTS installed in the chamber, bolted to the top of each of the three Aluminum I-beams. The height of the upper rotor above the floor of the chamber was 127.25 inches.

Test Procedure

Sonic anemometer, camera, and accelerometer signals were all monitored from a staging area north of the test chamber. Prior to the start of each point, analog data collection was initiated at the Astro-Med. Each point began with the rotor operator energizing the motor system. A live tuft image was reviewed (on the laptop outside the chamber) to verify that flow inside the chamber was quiescent and the number of tangled tufts was acceptable. Once the tufts were no longer moving, the Test Director ordered the sonic anemometer digital velocity measurement to begin. Twenty seconds later the time-lapse photography was initiated and an additional 10 seconds later the rotor was started.

The rotor operator ramped up in an approximately linear fashion to the desired operating RPM while speeding through the natural frequencies of the system to avoid excessive vibration. Once near the desired operating RPM, the operator leveled off the RPM. A typical data point therefore spans three regimes: a 30-second quiescent period wherein the system has been energized but the rotor is not spinning (to acquire baseline recirculation velocities); an approximately 30-second run-up from quiescent to desired RPM; and finally a 2-minute period at constant RPM.

At the end of the test point, analog data acquisition at the Astro-Med stopped, followed by digital velocity measurements at the laptop. Finally, the rotor was brought to rest. Image acquisition had already self-terminated after the acquisition of 21 images. Power to the rotor test stand was turned off at the RCC and the PAD opened to allow personnel to free any tangled tufts prior to the next data point. If entry needed less than 2 minutes or so, the UV lamps were left on (for efficiency). Once turned off, the UV lamps required several minutes to reach peak UV output. On leaving the chamber the PAD was re-closed.

Two MRTS test stand locations are called for in the Test Matrix in Table 1. The first test stand location was the chamber centerline as shown in Figure 14. The original plan had been to install the tuft frame at the far side of the chamber in order to place it as far as possible from the PAD. This position was chosen to reduce the possibility of damage from personnel entering or leaving the chamber. This was not possible because of the two missing floor panels at the desired location and the presence of the I-beams mounted on top of the raised hard points (Figs. 11–13). The decision was therefore made to locate the tuft frame 180 degrees from the original location inside the chamber, placing it directly inside the 25-foot- diameter access door as shown in Figure 14. Installation of the MRTS on top of the four hard points on the floor caused interference with the tuft frame, requiring the tuft frame to be mounted on top of four, 12-inch-high wooden blocks wrapped in Amerstat film as shown. The tuft frame was still able to roll underneath the blast shield as planned. In hindsight, the alternative location chosen for the tuft frame was a poor decision. Not only did it force personnel to squeeze past the tuft grid to gain access to the chamber through the PAD to free tangled tufts at the end of each data point, but the proximity of the tuft grid to the PAD resulted in a breeze that tended to re-tangle tufts as soon as they were freed. This was a constant problem throughout the test.

12

The sonic anemometer stand is shown positioned on the floor. The stand offered sufficient flexibility in positioning the sonic anemometer so that no shimming was required. Positive directions in the rotor coordinate system for radial direction, vertical direction, and azimuthal direction are shown in Figure 15. The sonic anemometer is shown installed at the 75-percent radial station *beneath* the rotor plane, indicating a thrust = down, wake = up configuration.

Figure 16 shows the MRTS installed 2m off-axis in the Space Simulator. The tuft frame was left in its original position and is no longer adjacent to the MRTS. The Aluminum I-beam close to the chamber centerline has been removed, and the tuft frame is no longer supported on wooden blocks. Tufts are therefore 1 foot closer to the chamber floor than for testing with MRTS on the chamber centerline. Note the location and orientation of the sonic anemometer stand.

Test Matrix

WT-1 consists of six runs, each containing four data points. Each run corresponds to a different experimental geometry, and each point within a run signifies a different target RPM starting from the rotor at rest. The experimental geometries for this test varied the MRTS location inside the chamber, thrust up/thrust down configuration, and sonic anemometer height above/below the rotor plane. The values for each point were 500, 1200, 1700, and 2000 RPM for runs 1–4, and 750, 1200, 1700, and 2000 RPM for runs 5 and 6. Two rap tests, one for the centered test stand and one for the off-axis test stand, were performed prior to rotor run-up at each of the respective test stand positions. The natural frequencies found from these tests were used to determine rotor RPM values to avoid during testing and account for the slightly different test RPMs chosen for the two test stand positions. The chosen RPMs were selected to avoid the natural frequencies of the system while still representing an even spread of RPM values within the motor operating range.

The complete test matrix is presented in Table 1. All the data presented in this report were acquired in two days of testing (12/16/2015 and 12/17/2015) between the hours of 10 a.m. and 8 p.m. PST.

Results and Discussion

The rotor thrust measurements presented in Figure 17 were part of the system checkout prior to shipment of the MRTS to JPL. They were not intended to be research-quality data and atmospheric pressure and air temperature were not recorded. Thrust measurements from two separate runs are presented. Making an educated guess for air density allows C_T to be estimated at 0.0215, independent of rotor RPM. Figure 17 shows thrust measurements made at Ames with steel blast shields installed (thrust = up, wake = down configuration) plotted against rotor RPM[2]. Higher than anticipated vibratory loads were encountered at JPL due to the relatively soft mount on the chamber floor. Load cells were therefore not installed during WT-1 testing at JPL in order to avoid possible damage.

The induced velocity through the rotor disk in hover, V_h, can be determined from

$$V_h / V_{tip} = \sqrt{(C_T/2)} = 0.1467$$

independent of p, T, ρ, or chemical composition of the atmosphere.

For 2500 RPM, $V_{tip} = \Omega R = 436.4$ ft/sec giving $V_h = 64.0$ ft/sec = 19.5 m/s.

13

Rotor hover performance measurements are notoriously difficult to make inside a *closed* chamber. It is usually not difficult to ensure the rotor is operating out of ground effect by locating the rotor sufficiently high above the floor (and sufficiently low beneath the ceiling). If measurements are made before the recirculation reaches the rotor, one may hope to get true "free-air" hover performance. Unfortunately, it takes time to adjust RPM and simultaneously avoid the resonant frequencies of the test stand, so the recirculation may reach the rotor before the rotor reaches the desired rotor RPM. After the recirculation starts to be entrained into the rotor disk, measurements are actually being made in a slow climb, where the climb velocity can be estimated from the average velocity of recirculation towards the rotor. True hover chambers usually avoid problems with recirculation by discharging the rotor wake (and entraining fresh fluid from below the rotor).

A simple estimate for the average recirculation velocity towards the rotor can be obtained by equating the mass flow through the rotor disk, $\rho V_h A$, to the recirculation mass flow, $\rho V_{recirc} A_{ch}$, where A is the area of the rotor disk, A_{ch} is the area of cross-section of the chamber, and V_{recirc} is the average recirculation velocity.

For the WT-1 wind tunnel test, $D = 40$ inches and $A = 8.73$ square feet. The Solar Simulator chamber diameter is 25 feet resulting in $A_{ch} = 490.87$ square feet.

Hence,

$$V_{recirc} / V_h = A / A_{ch} = 0.018$$

The mean recirculation velocity averaged across the full chamber width is therefore estimated at a little under 2 percent of V_h.

No obvious differences in flow recirculation were discernible as a function of rotor RPM from examination of tuft images once on condition. Tuft images were selected for this report based on the number of tufts that remained untangled by the time the desired RPM was reached. If certain tufts were tangled prior to rotor spin-up, they remained tangled for the duration of the data point. More tufts became tangled with the horizontal support threads as each data point continued. This indicates the importance of freeing as many tufts as possible before the start of the next run and illustrates the problem with having the tuft frame adjacent to the PAD. Often, after tangled tufts were freed, they would become re-tangled before personnel could leave the chamber through the PAD.

The quiescent flow prior to rotor spin-up for Run1 Point1 is shown in Figure 18. For this data point the MRTS is located on the chamber centerline, and the tuft grid extends from the MRTS all the way to the chamber wall. The tuft frame is mounted atop 12-inch-high wooden blocks. The top row of tufts is clearly wrapped around the horizontal support thread and is of little value. The remaining tufts are hanging vertically downward, exhibiting no motion during the 2-second exposure. Tuft length is 5.0 inches. The camera was clearly not positioned optimally. The optical axis of the camera is clearly not perpendicular to the tuft frame, as called for in the test plan. The image therefore shows a certain amount of distortion that could easily have been avoided. Also, the right-hand column of tufts is completely blocked by the sonic anemometer stand hardware. Figure 19 illustrates the flow direction during Run1 Point1 once "on condition" at 500 RPM corresponding to thrust = down, wake = up. The top row of tufts is wrapped around the horizontal thread and the bottom row of tufts is stuck to the bottom of the frame. This is apparently due to adhesive remnants on the tufts from being taped down in storage for the trip to JPL. The tuft pattern shows a relatively smooth entrainment pattern. Tufts are pointing downward at the wall, toward the MRTS test stand in the middle, and then upward towards the rotor disk. The entrained flow is not steady, but only a relatively small amount of tuft motion is observed during the 2-second exposure.

Figure 20 is taken from Run4 Point1 corresponding to thrust = up, rotor wake = down. Many of the top row of tufts remain free in this image adding to the complete picture. The tuft pattern is clearly indicative of a ring vortex between the rotor plane and the chamber floor, encircling the test stand. Flow rotation extends from the wall to the test stand and from the floor to the rotor plane. Considerable tuft motion can be seen in the image, indicating a high level of turbulence, especially close to the test stand, where large amplitude tuft motion results in reduced tuft visibility.

With the MRTS moved 2m off-axis, Figure 21 illustrates quiescent flow prior to rotor start for Run5 Point1. All the tufts hang vertically downward because of gravity and exhibit no motion during the 2-second exposure. Note that the MRTS is no longer in the picture. The tuft frame is in its original position but the MRTS has moved 2m to the right. The tuft frame now rests on the chamber floor. Figure 22 is indicative of the mean velocity field during Run6 Point4 (thrust = up, wake = down) with the MRTS 2m off-axis. Fortunately most tufts are free to rotate providing a complete picture of the recirculation beneath the plane of the rotor. Once again, the tuft pattern is representative of a ring vortex between the plane of the rotor and the chamber floor, encircling the test stand. Flow is clearly directed downward close to the test stand, radially outward along the floor of the chamber and upward along the chamber wall. Flow rotation occupies the complete field of view. Run6 Point4 is a high-speed run (2000 RPM) and considerable tuft coning is evident indicating a high level of turbulence. The vortex center is clearly closer to the wall than to the rotor test stand.

CSAT3 sonic anemometer digital velocity time histories are presented in Appendix A for all three orthogonal velocity components in rotor coordinates.

A typical velocity measurement is shown in Figure 23 taken from Run3 Point4. Notice the initial 30-second-long quiescent state followed by linear ramp-up in rotor RPM as a function of time and a final 2-minute "on condition" at 2000 RPM. Run3 Point4 corresponds to thrust = up, wake = down configuration with velocity being measured 19.5 inches above the upper rotor close to the 75-percent radial station. The measured Vz indicated in Figure 23 is downward towards the rotor plane, in the negative z-direction as expected. The rotor wake is known to contract as it passes through the rotor disk. Vr is shown toward the rotor hub in the negative r-direction, indicating flow towards the rotor axis as anticipated. The direction of hub rotation for thrust = up is counterclockwise when viewed from above, in the positive $V\theta$ direction. Any pre-swirl produced in the flow upstream of the rotor plane is therefore also expected to be in the counterclockwise direction. $V\theta$ is positive, as expected.

Table 2 presents a summary of the sonic anemometer velocity measurements made during the test. Both mean velocities and standard deviations about the mean are tabulated for all three orthogonal velocity components in rotor coordinates, computed once "on condition" and after the assumed arrival of the rotor wake (based on large amplitude fluctuations in the anemometer signal). An example of the relative turbulence intensity in the axial direction of the rotor is shown in Figure 24 for the thrust = up configuration using data from Run3 and Run4. Two sets of data are shown corresponding to two locations of the anemometer above the upper rotor. Streamline contraction (acceleration of the flow) results in lower relative turbulence intensity in the axial direction as the rotor disk is approached.

Conclusions

Despite the extremely tight timetable that Ames personnel were given in order to meet the JPL testing schedule that was due to start in January of 2016, all the primary goals were achieved.

Fluorescent micro-tufts successfully revealed the ambient flow direction inside the hover chamber, albeit at atmospheric pressure, and demonstrated the advantage of testing the inverted rotor compared to testing the upright rotor. An upright rotor (thrust = up, wake = down) was shown to operate with a ring vortex between the plane of the rotor and the chamber floor.

Sonic anemometer velocity measurements were made on the intake side of the rotor close to the 75-percent radial station for both thrust up/wake down and thrust down/wake up configurations. These measurements were made both on the chamber centerline and 2m off-axis, and allow the determination of turbulence levels entrained into the rotor disk for both upright and inverted rotor configurations. Individual velocity time histories are helpful in documenting the typical turbulent gust to expect in the chamber due to recirculation and ensure that the control authority for the MSH is sufficient for free flight inside the Space Simulator.

The chamber was not evacuated down to Mars-like atmospheric pressures, so the operational limit of the sonic anemometer was not determined.

References

1. Brown, D.: NASA Announces Mars 2020 Rover Payload to Explore the Red Planet as Never Before. NASA Press Release 14-208, July 31, 2014.

2. Young, L. A.; Aiken, E. W.; Derby, M. R.; Demblewski, R.; and Navarrete, J.: Experimental Investigation and Demonstration of Rotary-Wing Technologies for Flight in the Atmosphere of Mars. 58th Annual Forum of the American Helicopter Society International, Montreal, Canada, June 11–13, 2002.

3. Young, L. A.; Aiken, E. W.; Gulick, V.; Mancinelli, R.; and Briggs, G. A.: Rotorcraft as Mars Scouts. IEEE Aerospace Conference, Big Sky, MT, Mar. 9–16, 2002.

4. Landau, E.: Helicopter Could be 'Scout' for Mars Rovers. NASA/JPL News Release 2015-031, Jan. 22, 2015.

5. Rajagopalan, R. G.; Baskaran, V.; Hollingsworth, A.; Lestari, A.; Garrick, D.; Solis, E.; and Hagerty, B.: RotCFD – A Tool for Aerodynamic Interference of Rotors: Validation and Capabilities. American Helicopter Society Future Vertical Lift Aircraft Design Conference, San Francisco, CA, Jan. 18–20, 2012.

Table 1. Test Matrix.

Run	Point	RPM	Test Stand Location	Thrust Direction	Sonic Anemometer Vertical Distance From Top Blade	Sonic Anemometer Radial Location
1	1	500	Center of Chamber	Down	20 in. below	15 in.
	2	1200	Center of Chamber	Down	20 in. below	15 in.
	3	1700	Center of Chamber	Down	20 in. below	15 in.
	4	2000	Center of Chamber	Down	20 in. below	15 in.
2	1	500	Center of Chamber	Down	40 in. below	15.375 in.
	2	1200	Center of Chamber	Down	40 in. below	15.375 in.
	3	1700	Center of Chamber	Down	40 in. below	15.375 in.
	4	2000	Center of Chamber	Down	40 in. below	15.375 in.
3	1	500	Center of Chamber	Up	19.5 in. above	15 in.
	2	1200	Center of Chamber	Up	19.5 in. above	15 in.
	3	1700	Center of Chamber	Up	19.5 in. above	15 in.
	4	2000	Center of Chamber	Up	19.5 in. above	15 in.
4	1	500	Center of Chamber	Up	39.75 in. above	15 in.
	2	1200	Center of Chamber	Up	39.75 in. above	15 in.
	3	1700	Center of Chamber	Up	39.75 in. above	15 in.
	4	2000	Center of Chamber	Up	39.75 in. above	15 in.
5	1	750	2 Meters East	Up	20 in. above	15 in.
	2	1200	2 Meters East	Up	20 in. above	15 in.
	3	1700	2 Meters East	Up	20 in. above	15 in.
	4	2000	2 Meters East	Up	20 in. above	15 in.
6	1	750	2 Meters East	Up	39.5 in. above	15.125 in.
	2	1200	2 Meters East	Up	39.5 in. above	15.125 in.
	3	1700	2 Meters East	Up	39.5 in. above	15.125 in.
	4	2000	2 Meters East	Up	39.5 in. above	15.125 in.

Table 2. Sonic Anemometer Velocity Measurements.

| Run # | Point # | Sonic Anemometer Velocity Measurements (m/s) | | | | | |
| | | Mean Velocity Components | | | Standard Deviations | | |
		V_r	V_Θ	V_z	σ_r	σ_Θ	σ_z
1	1	–0.316	–0.017	1.030	0.263	0.207	0.109
	2	–1.198	–0.024	2.427	0.594	0.712	0.449
	3	–1.635	–0.135	3.455	0.984	1.011	0.687
	4	–2.202	0.226	3.975	1.139	1.414	0.890
2	1	–0.040	0.001	0.257	0.143	0.158	0.126
	2	–0.317	0.210	0.517	0.396	0.550	0.336
	3	–0.578	0.040	0.643	0.577	0.672	0.505
	4	–0.536	0.285	0.676	0.802	0.909	0.571
3	1	–0.536	0.513	–0.899	0.326	0.240	0.205
	2	–1.394	1.038	–2.418	0.754	0.671	0.527
	3	–1.756	1.445	–3.606	1.051	0.933	0.757
	4	–2.071	1.614	–4.319	1.236	1.165	0.877
4	1	–0.072	0.133	–0.497	0.204	0.174	0.139
	2	–0.041	0.455	–1.093	0.477	0.570	0.382
	3	–0.255	0.706	–1.571	0.609	0.598	0.532
	4	–0.435	0.680	–1.940	0.715	0.717	0.553
5	1	–1.061	0.111	–1.608	0.303	0.295	0.207
	2	–1.626	-0.100	–2.745	0.463	0.523	0.348
	3	–2.238	0.223	–3.995	0.600	0.822	0.488
	4	–2.741	0.180	–4.611	0.697	0.722	0.517
6	1	–0.317	0.070	–0.749	0.222	0.239	0.137
	2	–0.476	0.113	–1.136	0.332	0.300	0.208
	3	–0.693	0.018	–1.792	0.342	0.347	0.275
	4	–0.822	0.342	–1.970	0.514	0.462	0.381
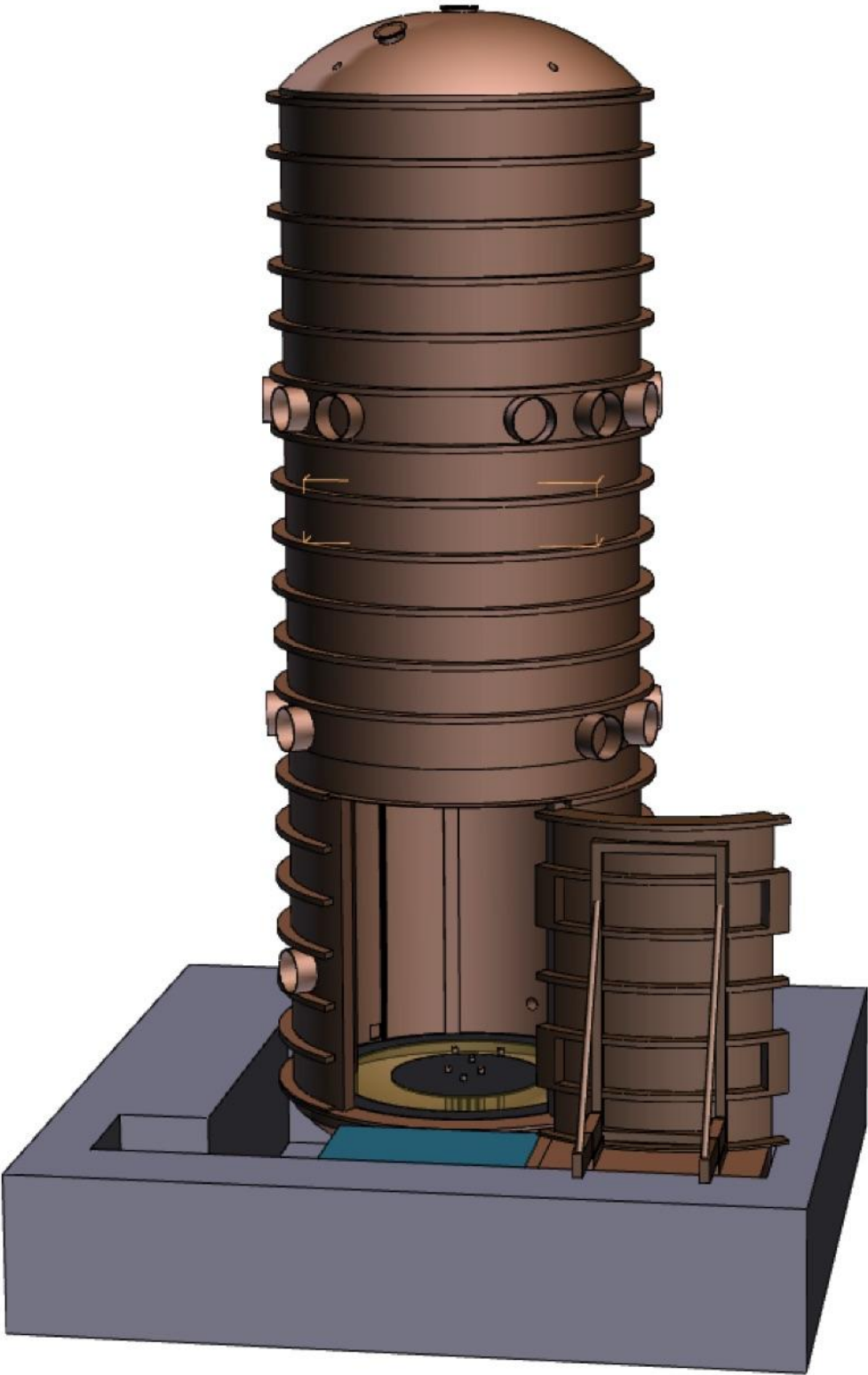
Figure 1. JPL 25-foot-diameter Space Simulator.
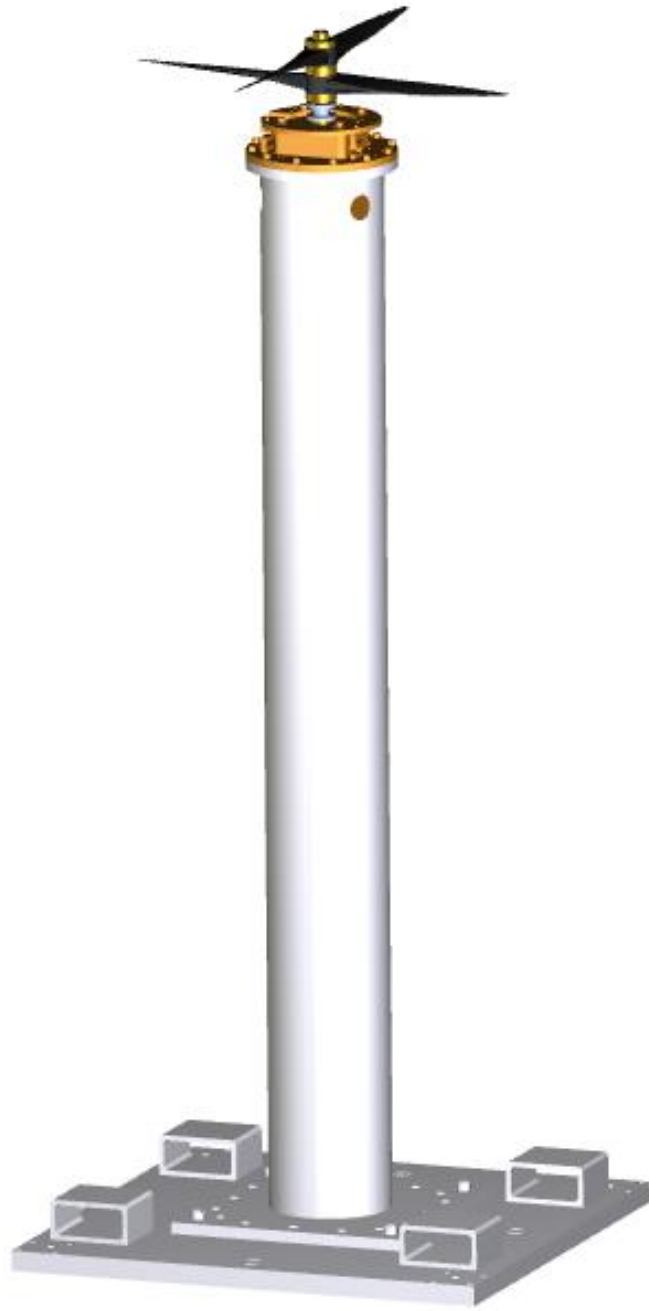
Figure 2. Mars Rotor Test Stand.
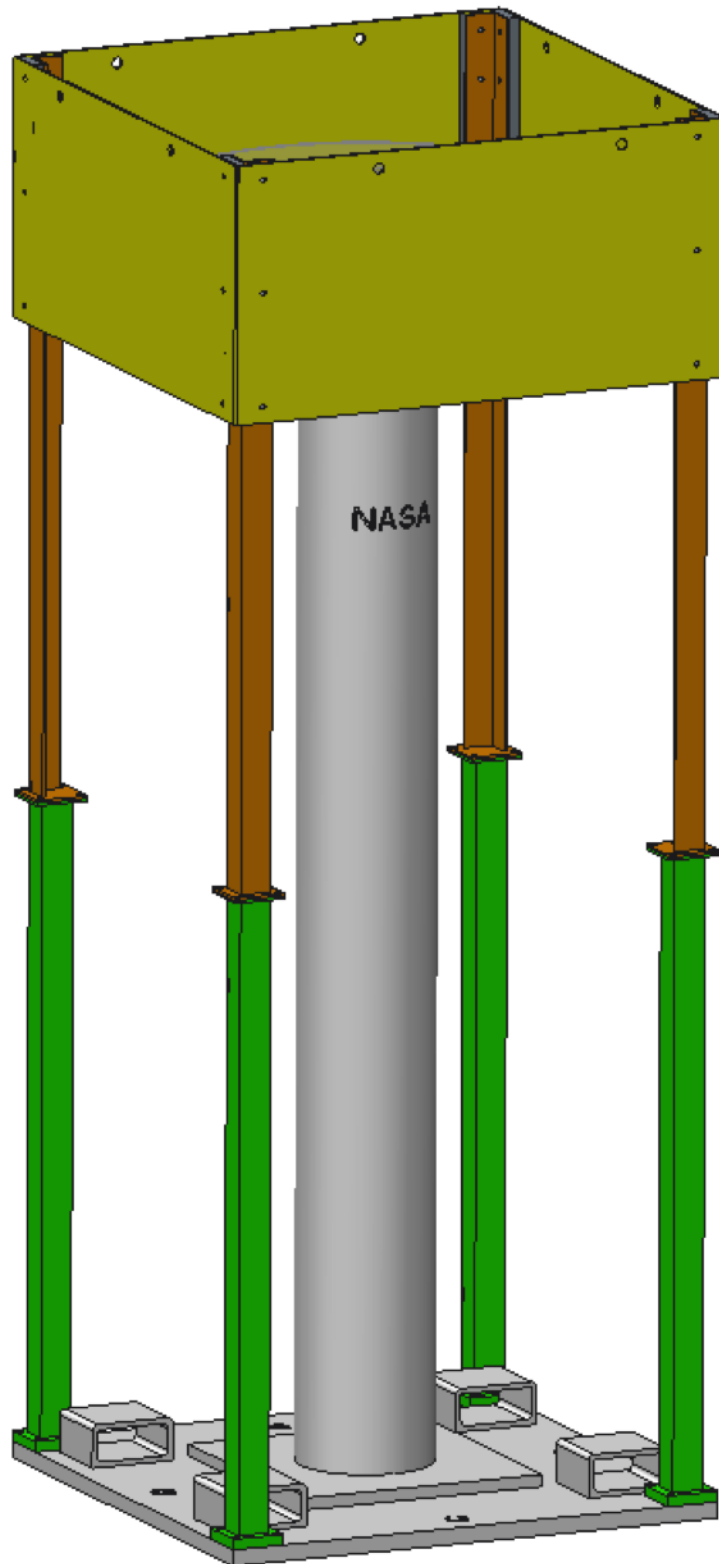
Figure 3. Sketch of MRTS with blast shield installed.

Figure 4. Single propeller and a pair of propellers in mounted orientation.
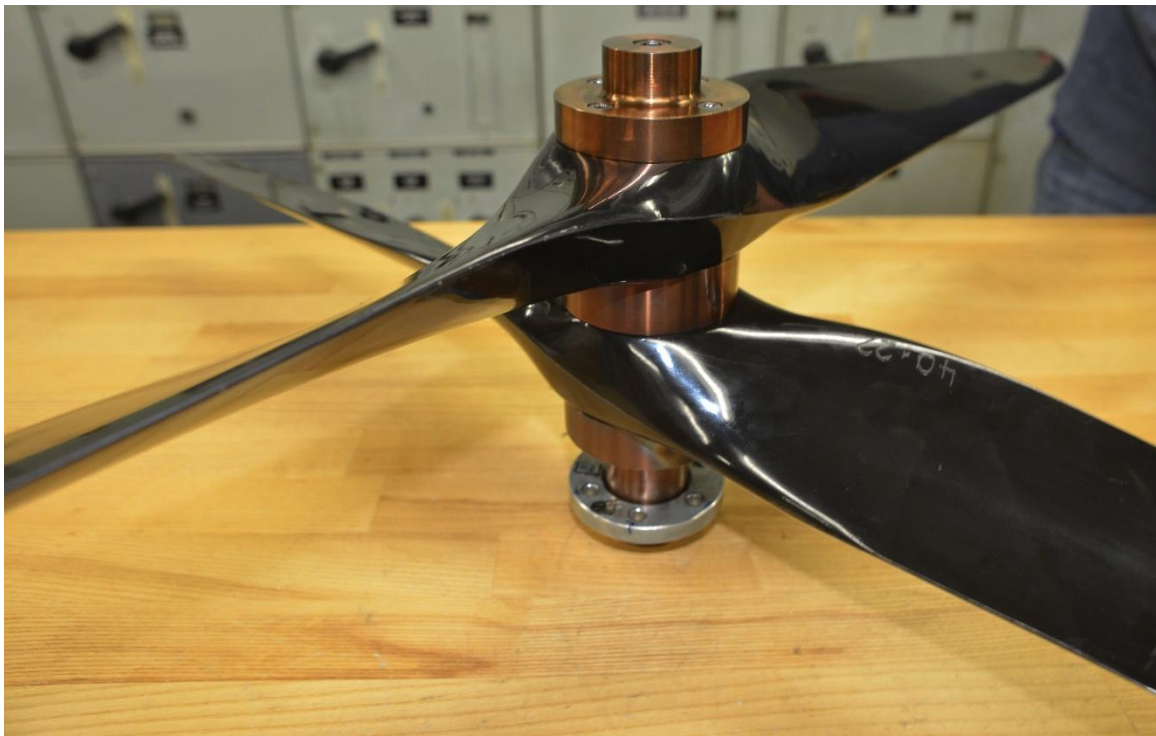
Figure 5. Hub assembly.
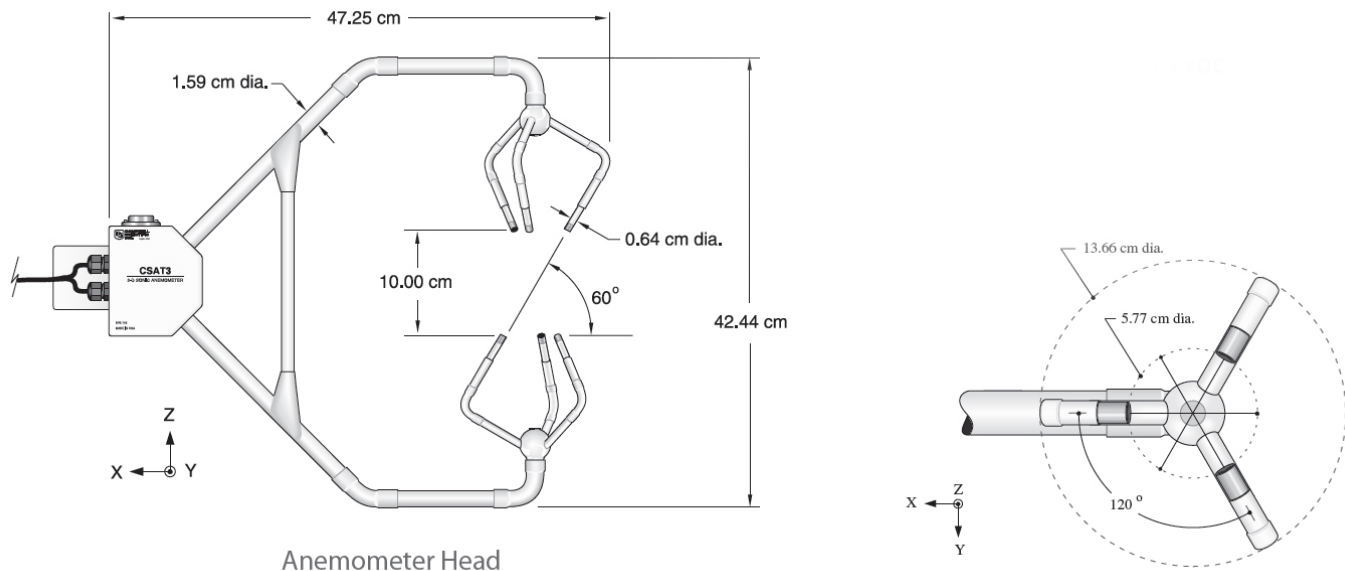
Figure 6. Sonic anemometer head with probe coordinate system.
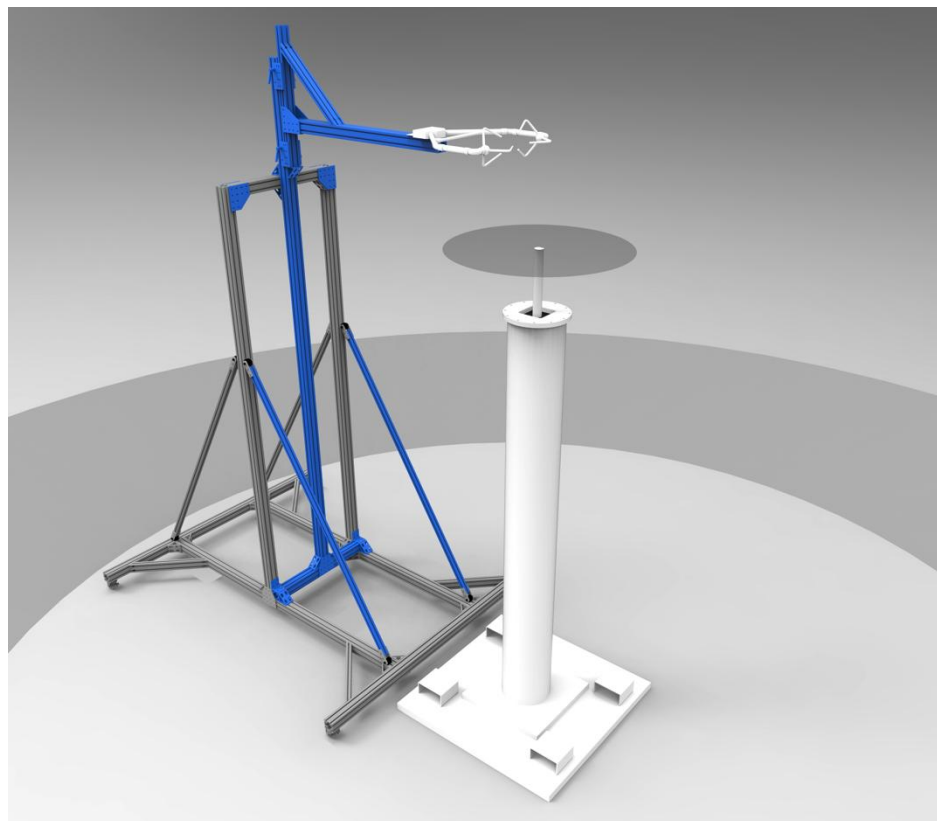
Figure 7. Sonic anemometer stand installed in Space Simulator.

Figure 8. Tuft frame (without tufts).
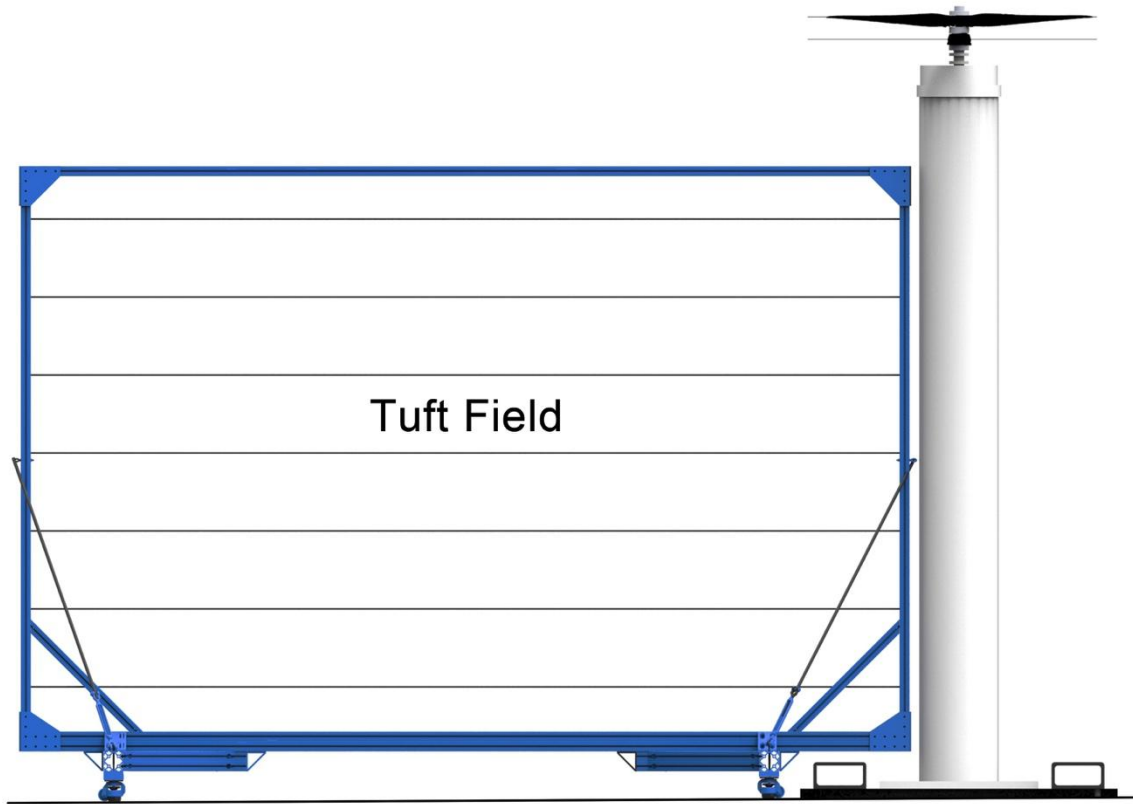
Figure 9. Tuft frame installation in chamber.
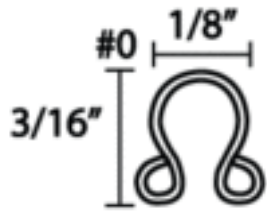
Figure 10. Micro-tuft mounting hardware (eyelet; fishing swivel with clasp).

Figure 11. Raised hard points in floor of Space Simulator.

Figure 12. Aluminum I-beams bolted to hard points in chamber floor.

Figure 13. MRTS assembly sans blast shield in Space Simulator.

Figure 14. MRTS mounted on centerline of Space Simulator.
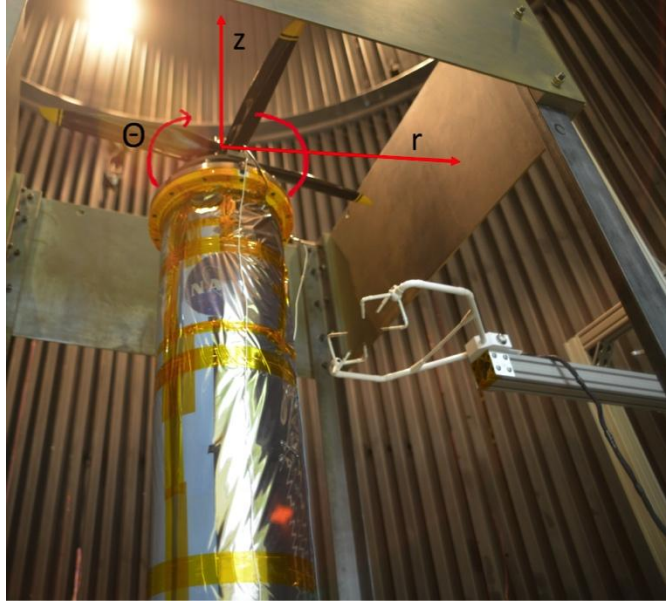
Figure 15. Rotor coordinate system.

Figure 16. MRTS mounted 2m off-center in Space Simulator.
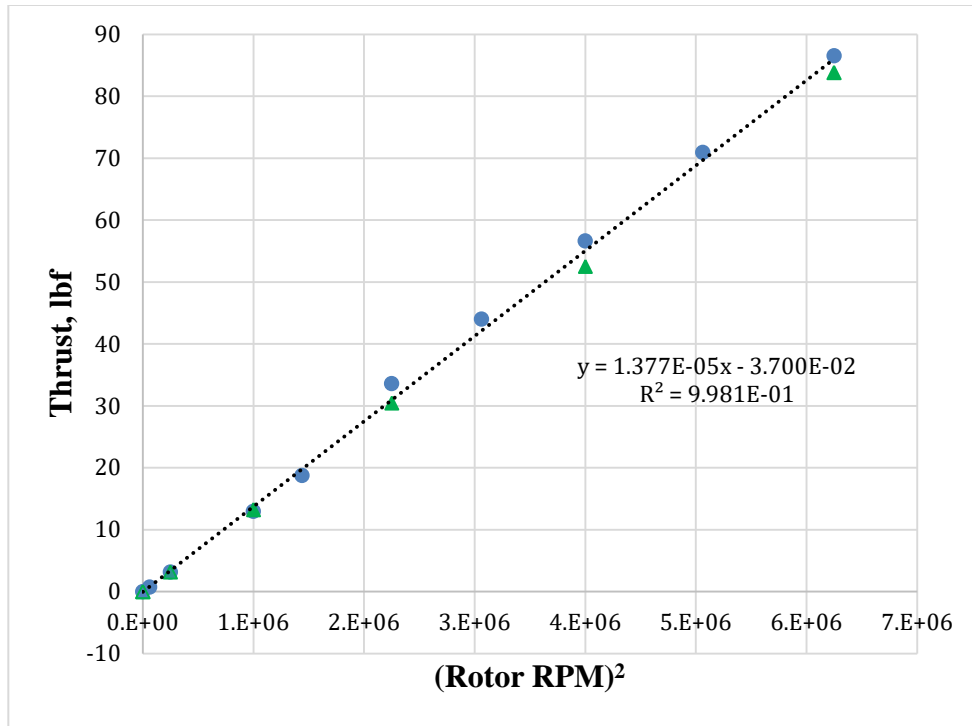
Figure 17. Rotor thrust measurement.

The equation and R^2 value shown on the chart:

$$y = 1.377E\text{-}05x - 3.700E\text{-}02$$
$$R^2 = 9.981E\text{-}01$$
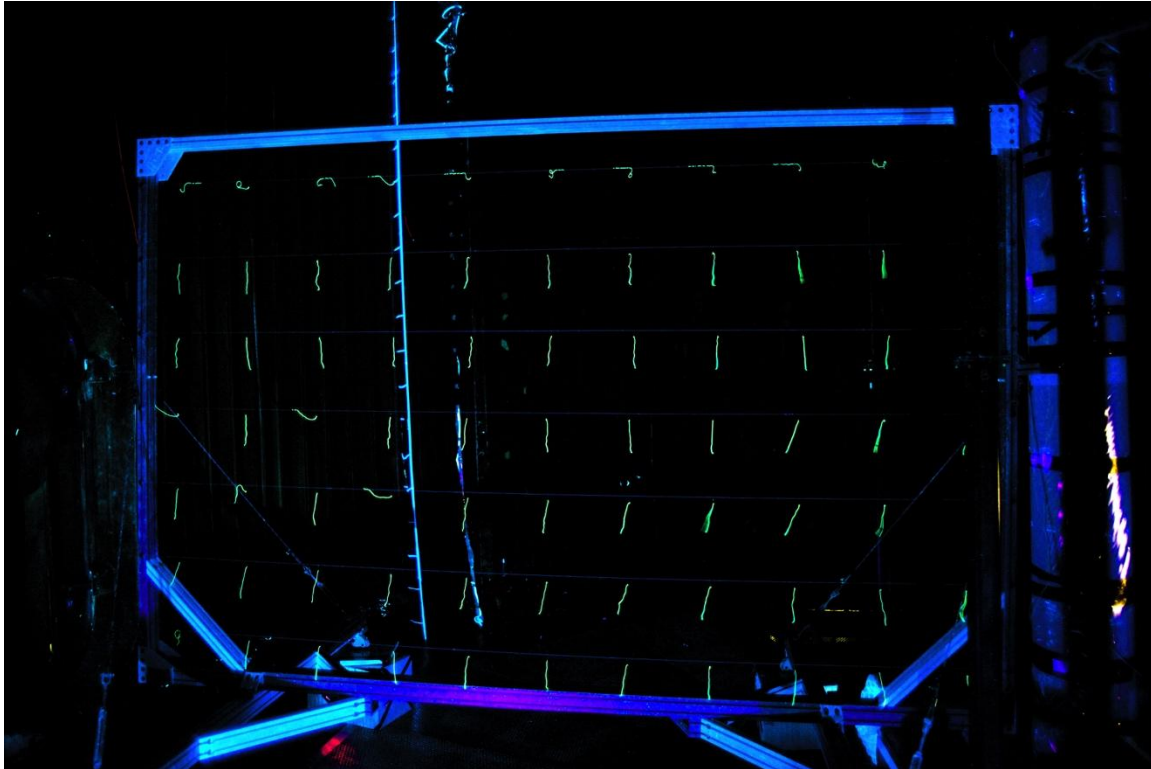
Figure 18. Quiescent flow prior to rotor spin-up for Run1 Point1.
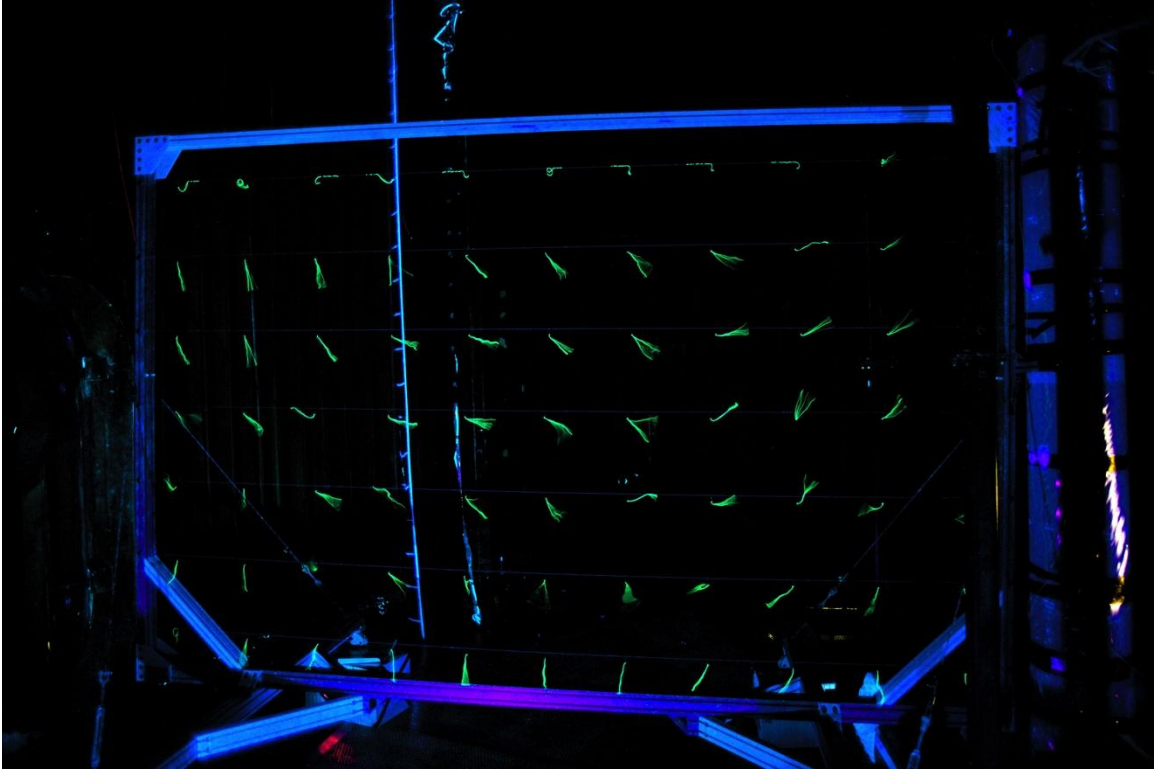
Figure 19. Tuft field during Run1 Point1 (thrust = down, wake = up).
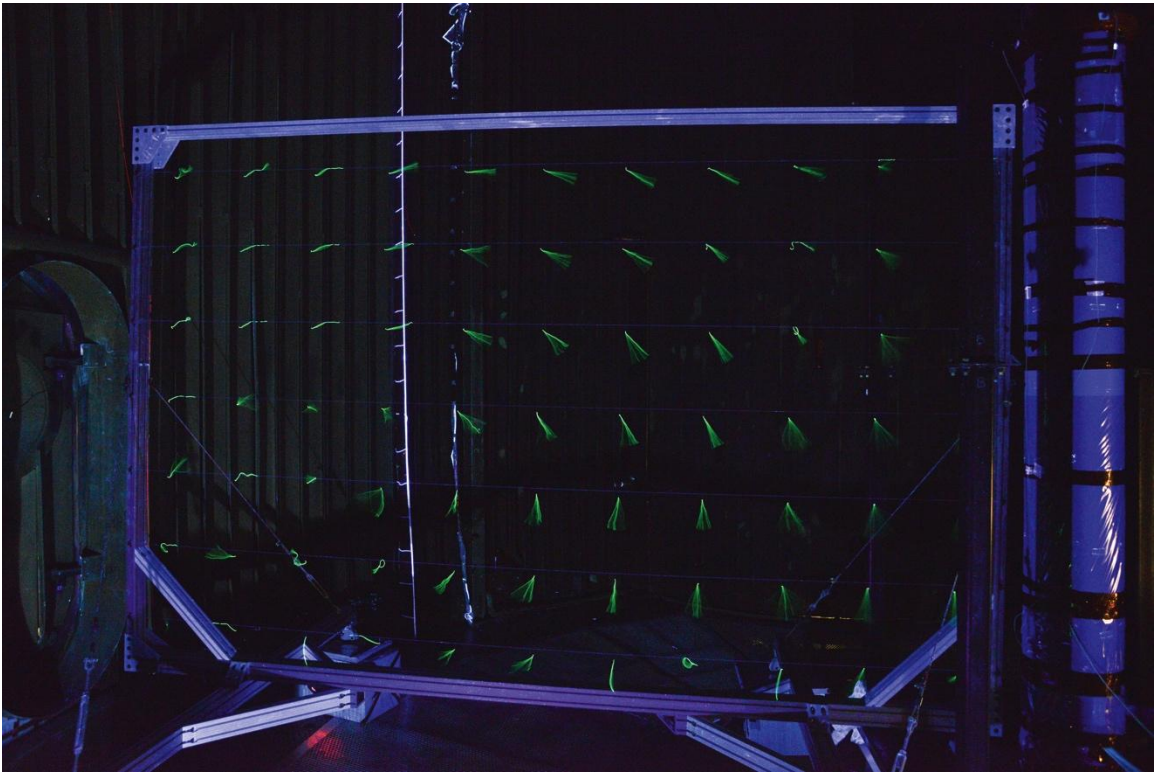
Figure 20. Tuft field during Run4 Point1 (thrust = up, wake = down).
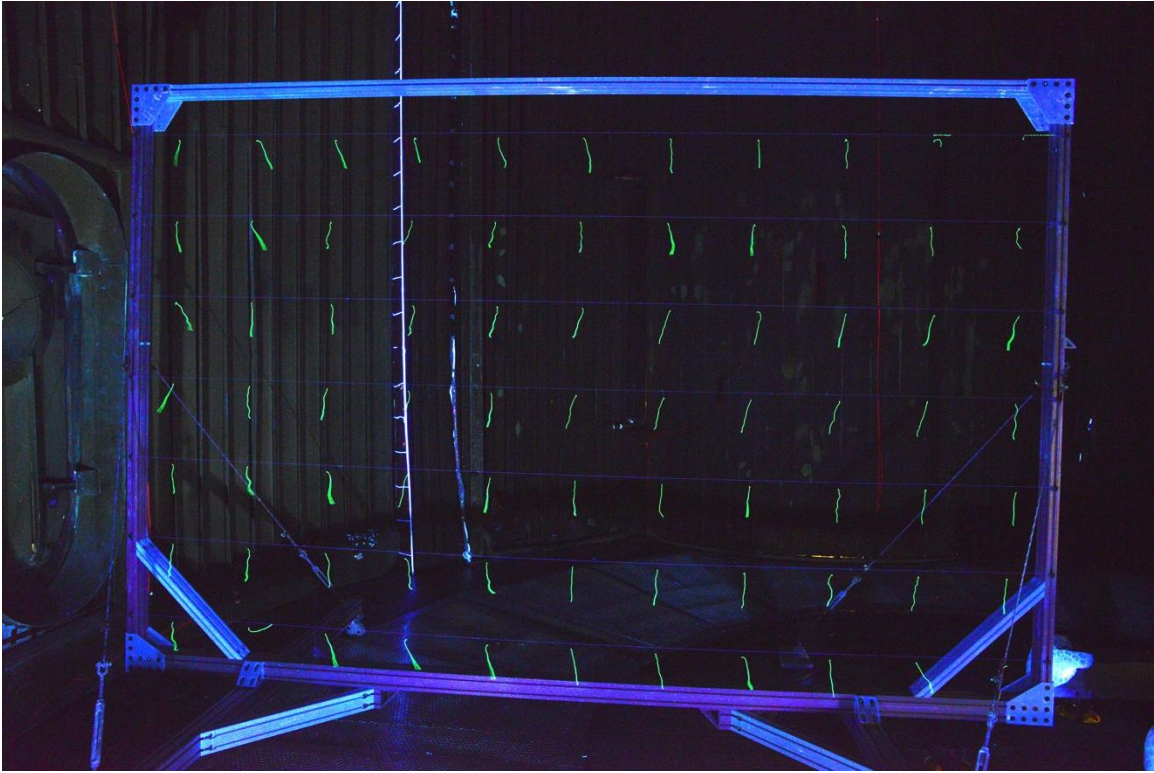
Figure 21. Tuft field prior to rotor spin-up for Run5 Point1.
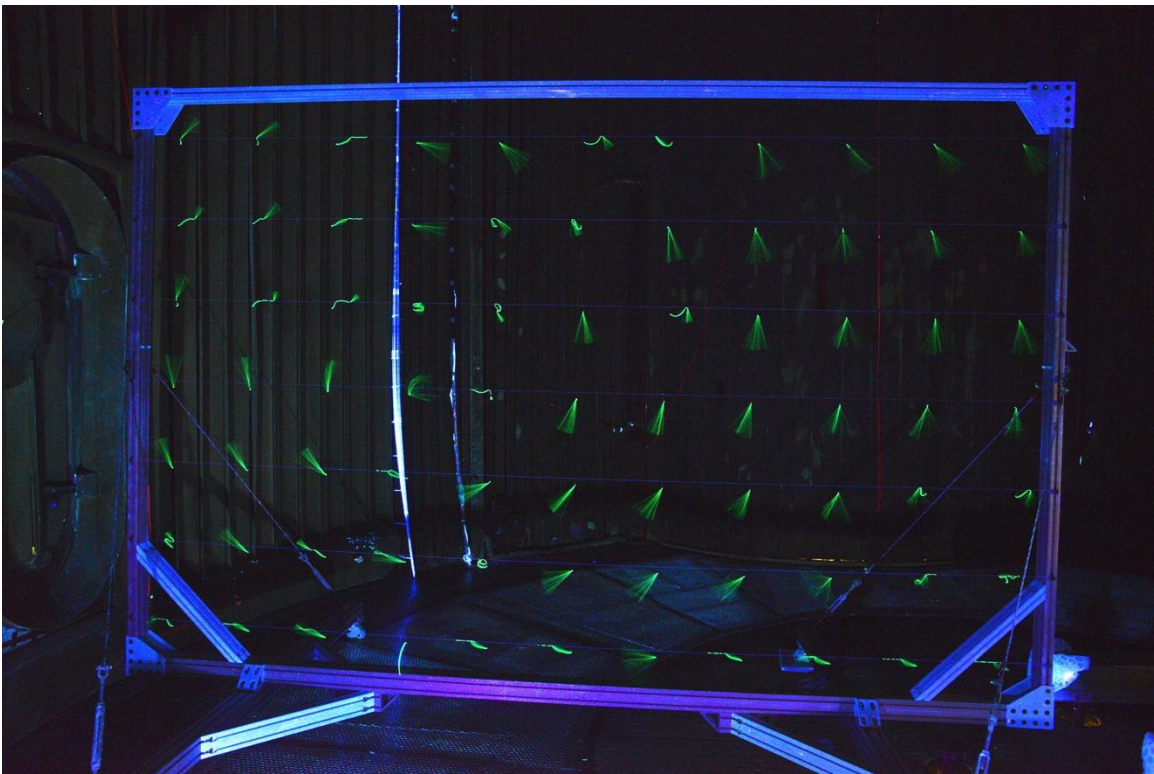
Figure 22. Tuft field during Run6 Point4 (thrust = up, wake = down).
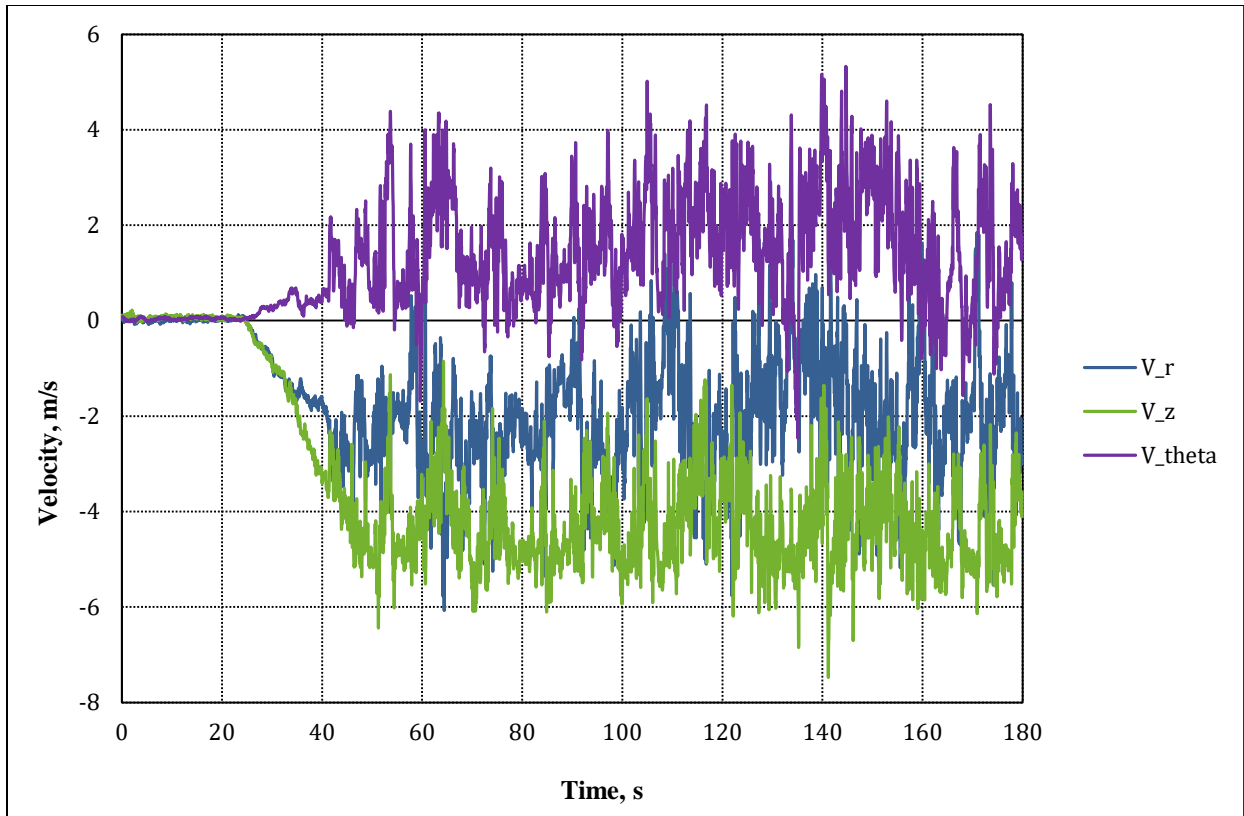
Figure 23. Typical velocity time history (Run3 Point4).
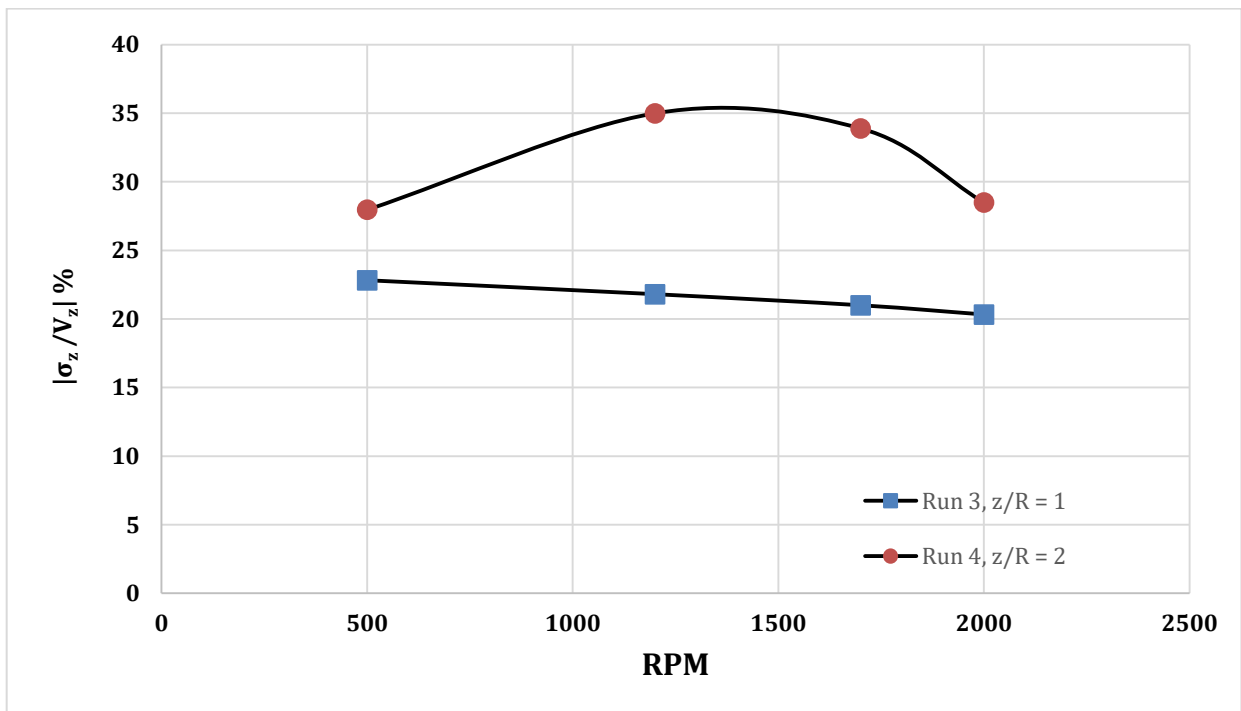
Figure 24. Turbulence level on entrainment side of rotor disk (thrust = up configuration).

32

Appendix A

Sonic Anemometer Velocity Measurements
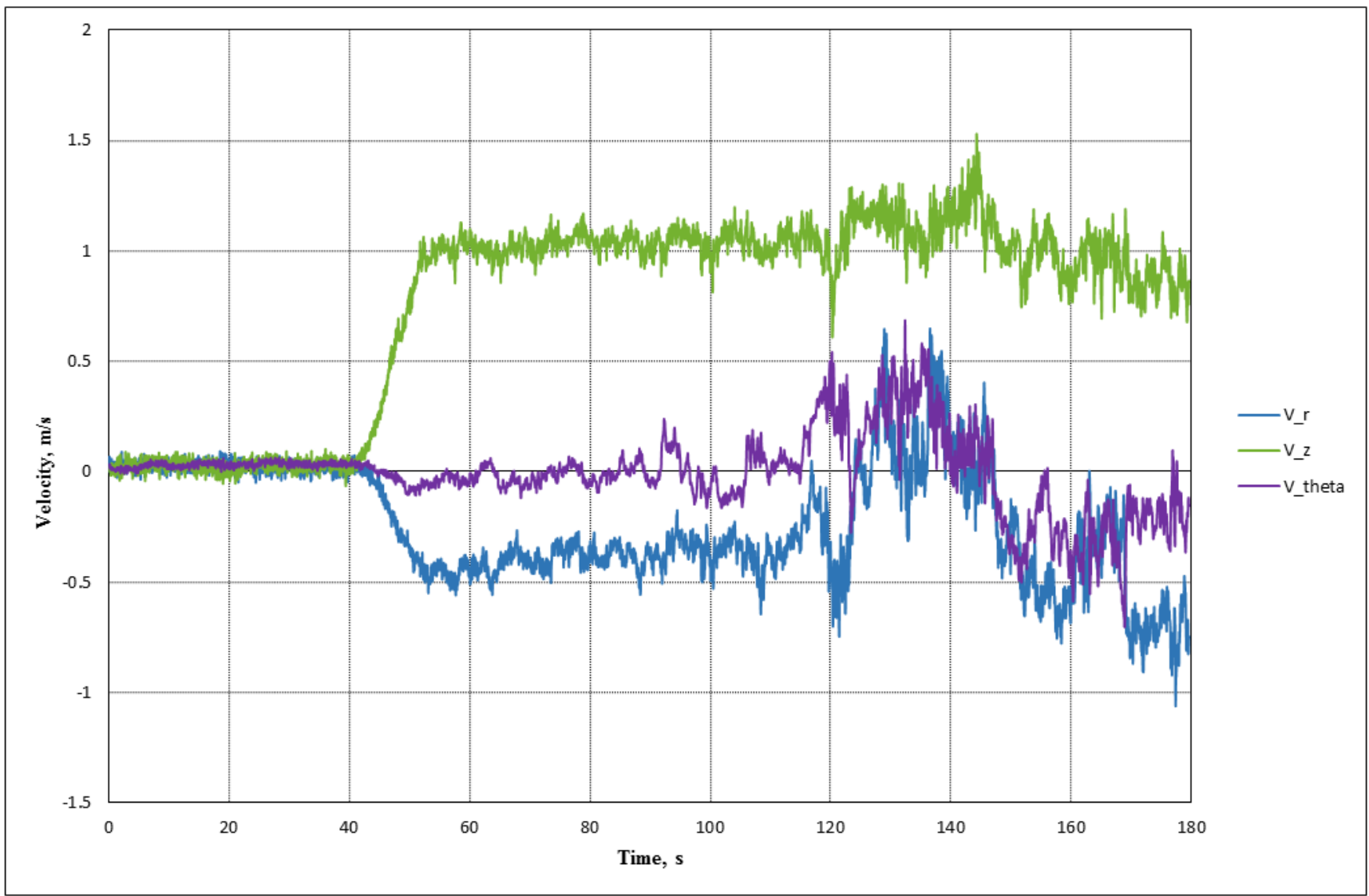
Figure A1. Run1, Point1 velocity data.
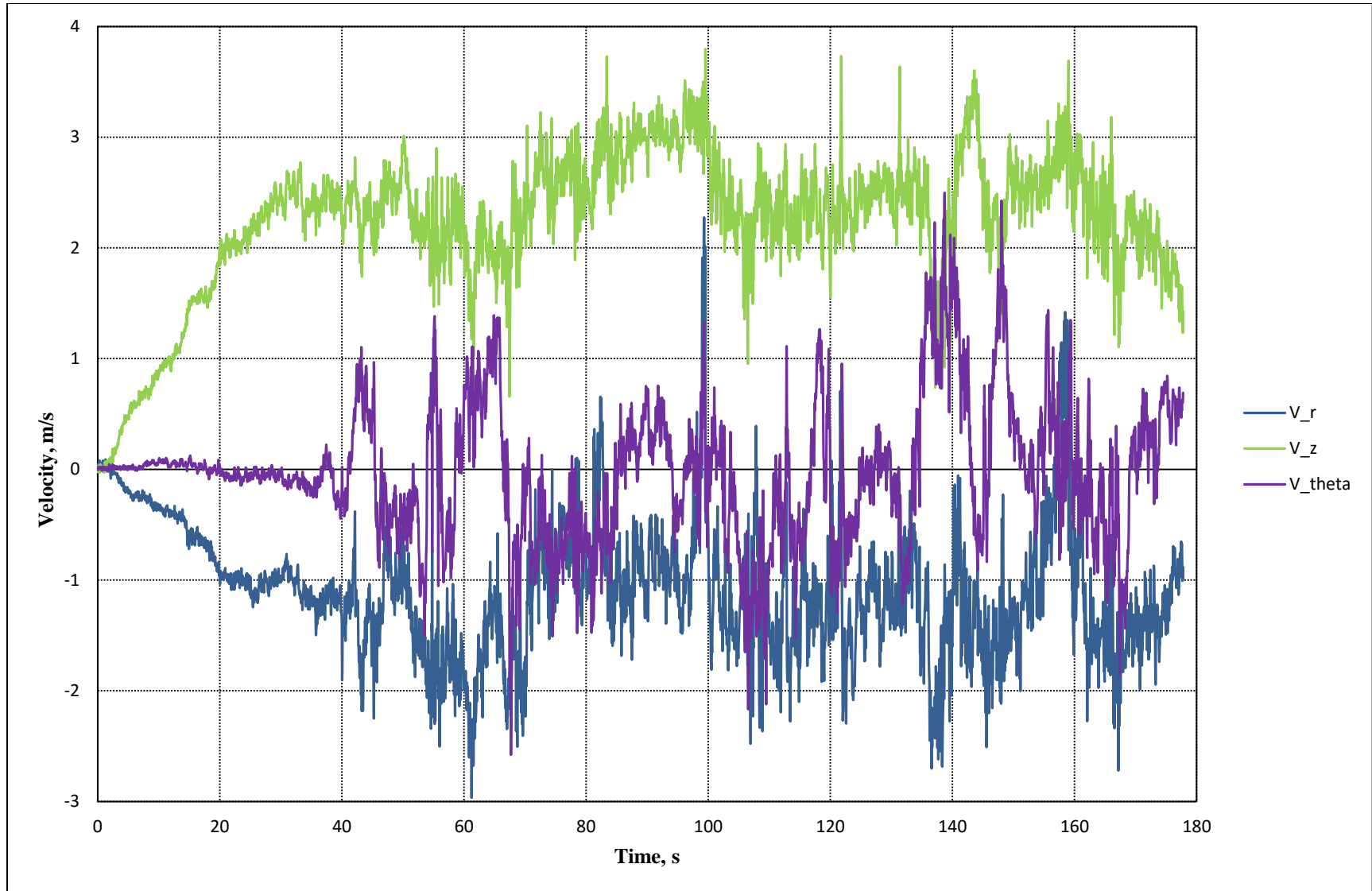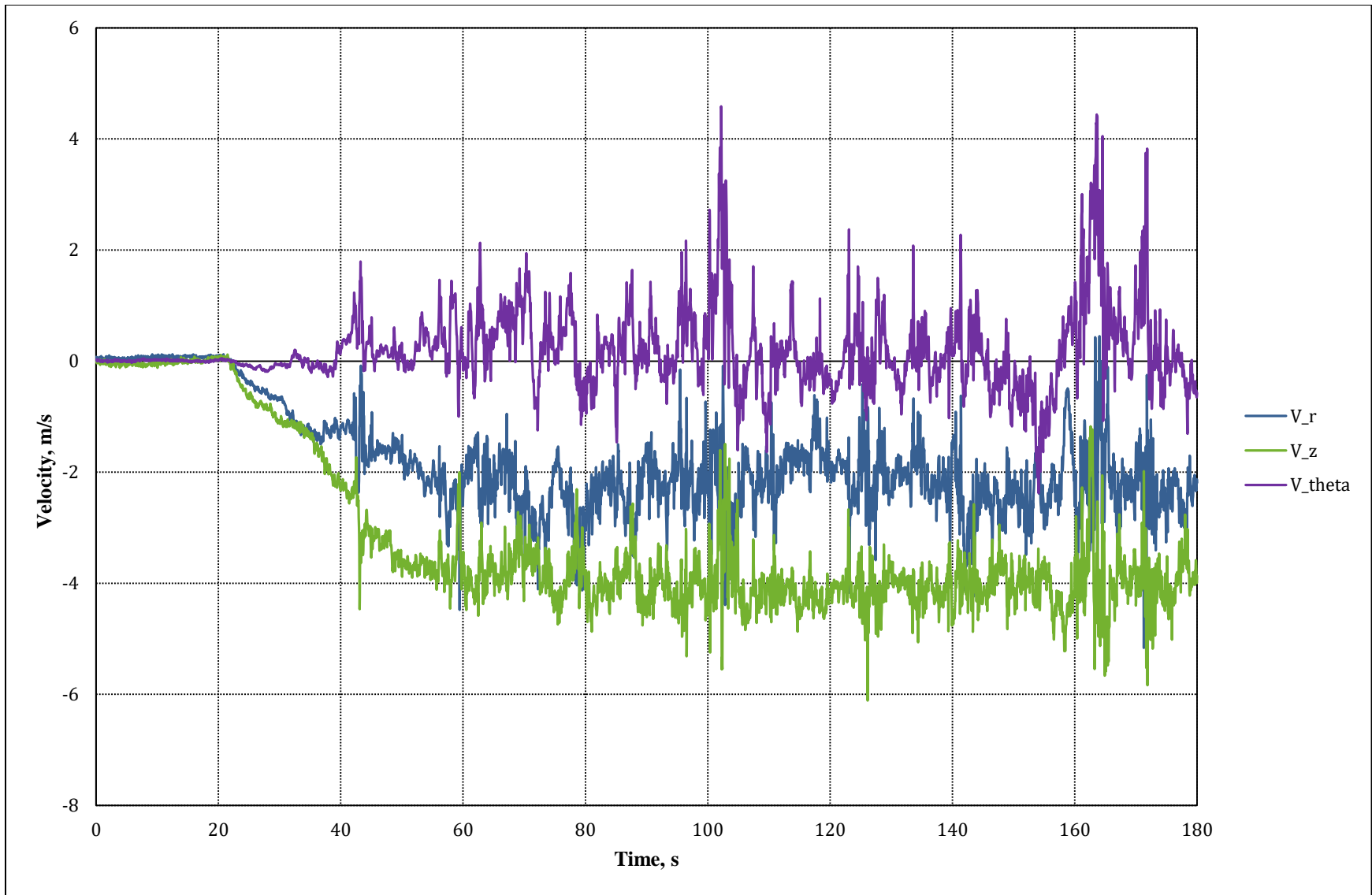
Figure A2. Run1, Point2 velocity data.
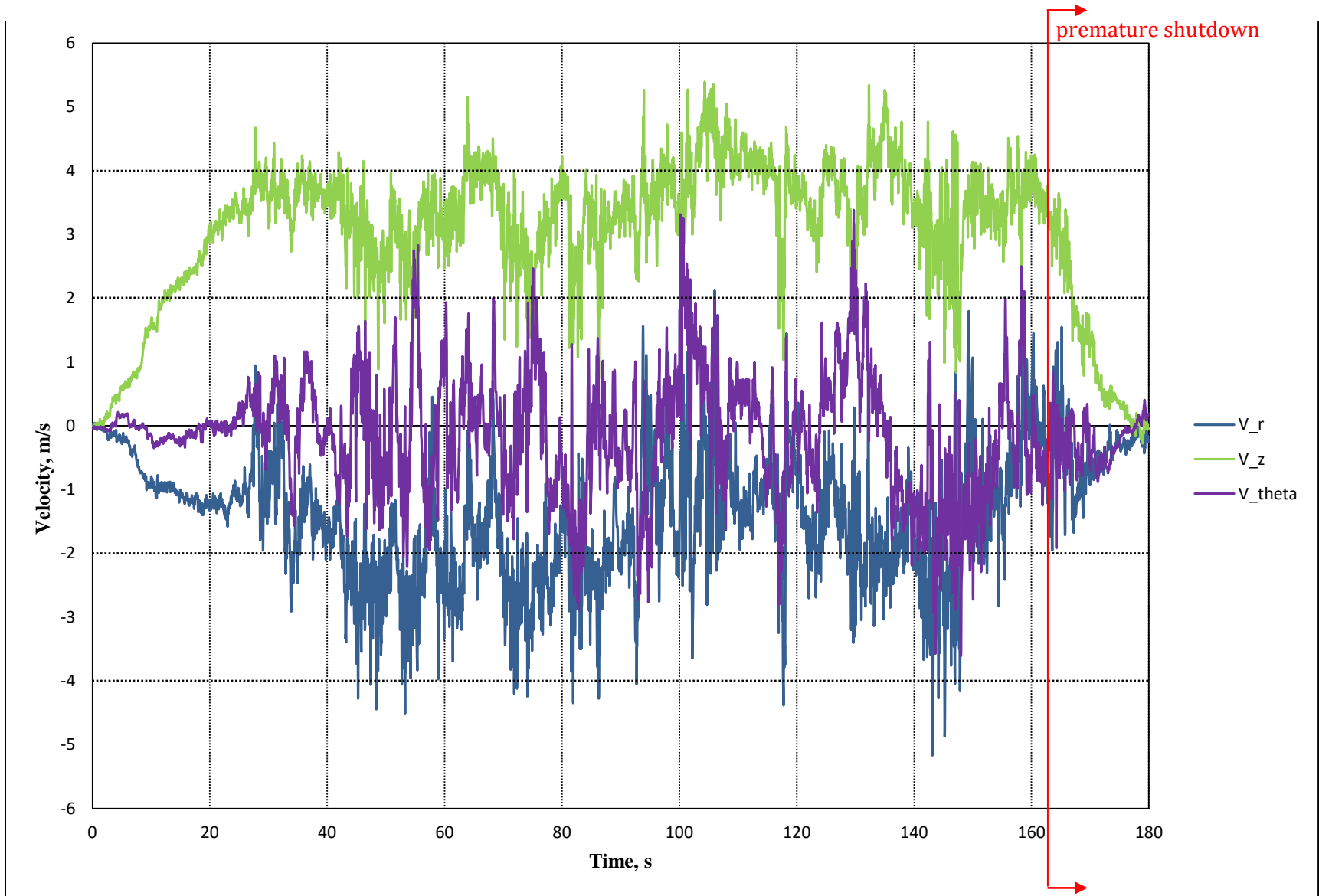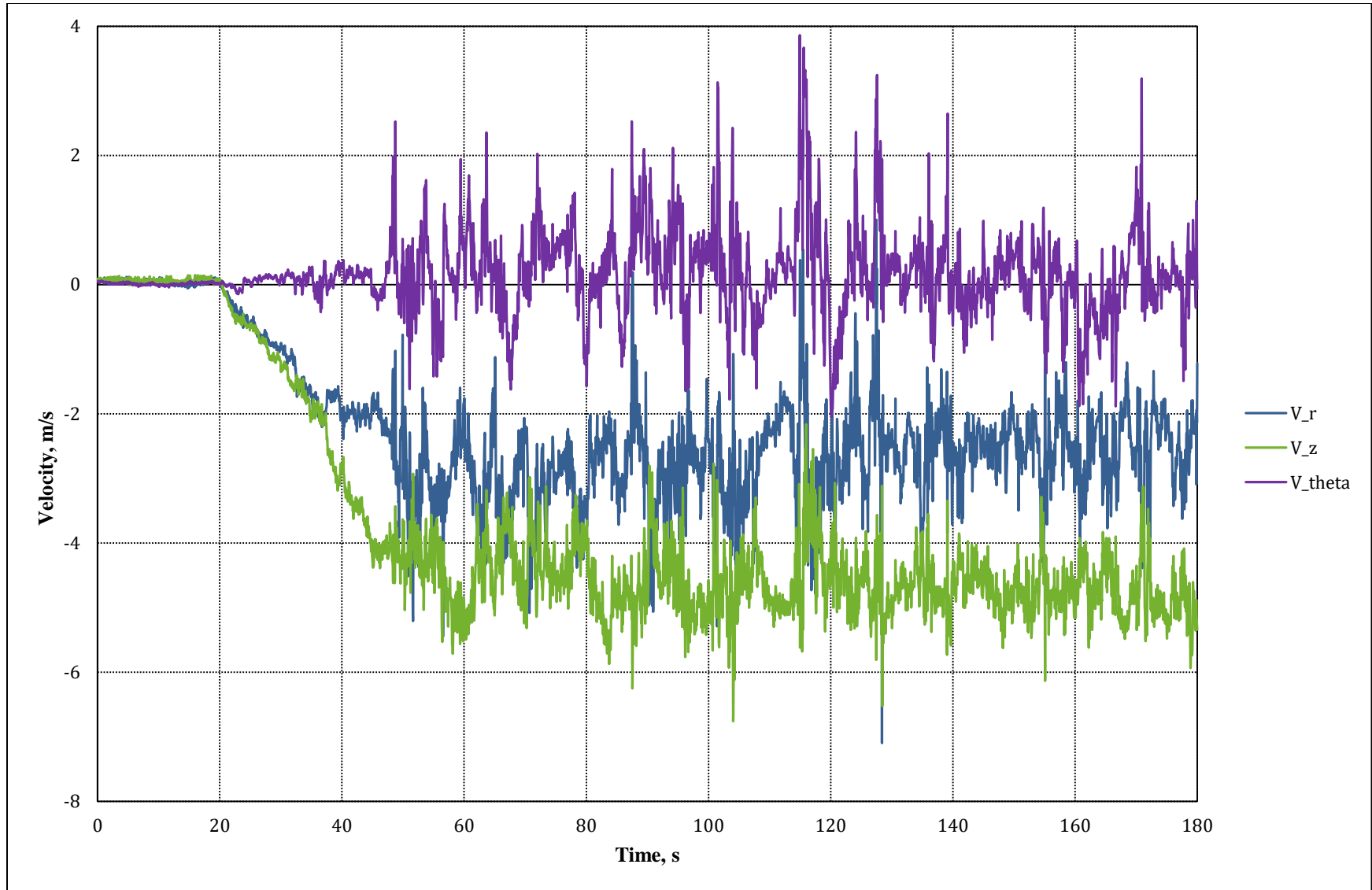
Figure A3. Run1, Point3 velocity data.
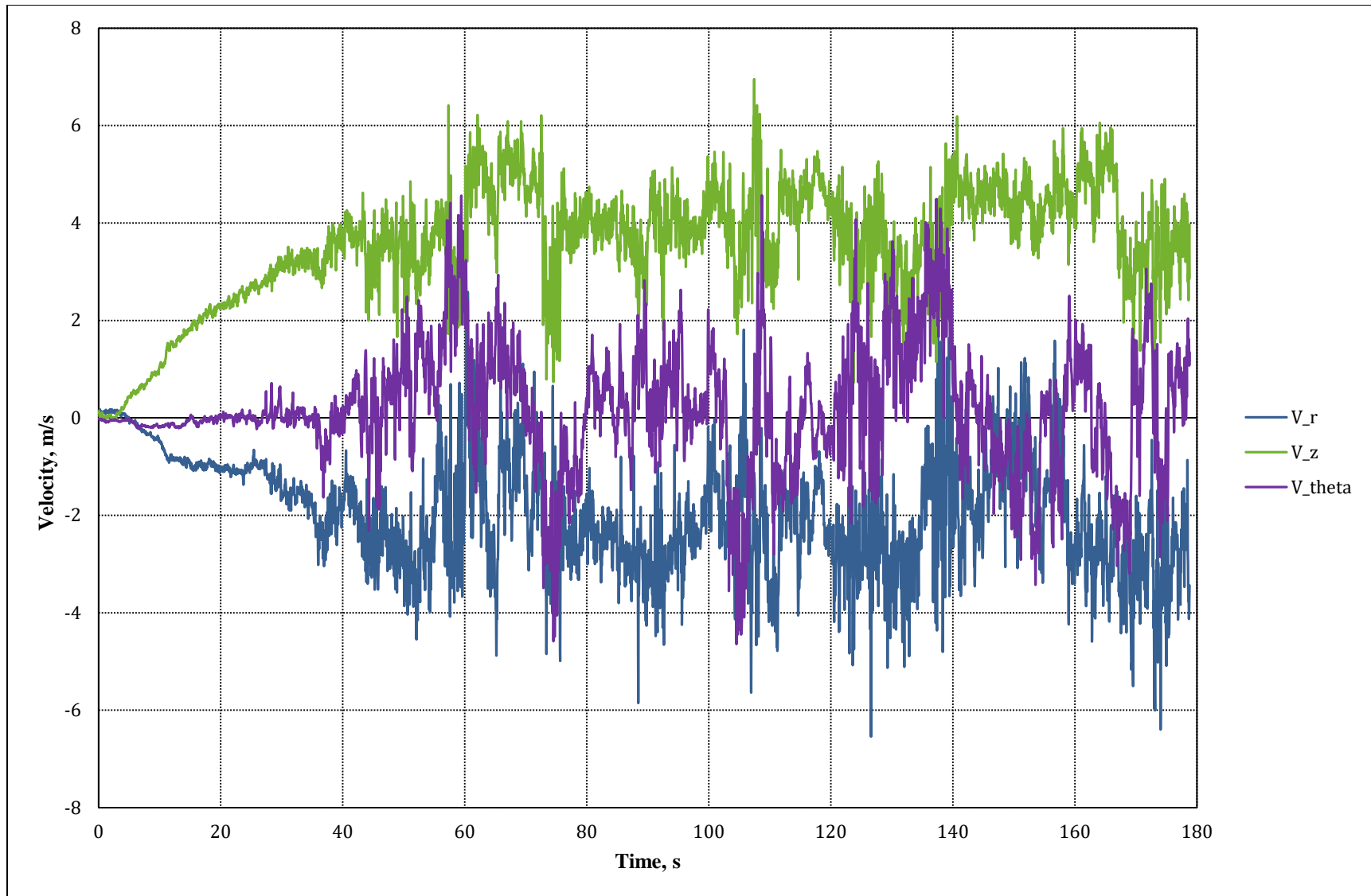
Figure A4. Run1, Point4 velocity data.
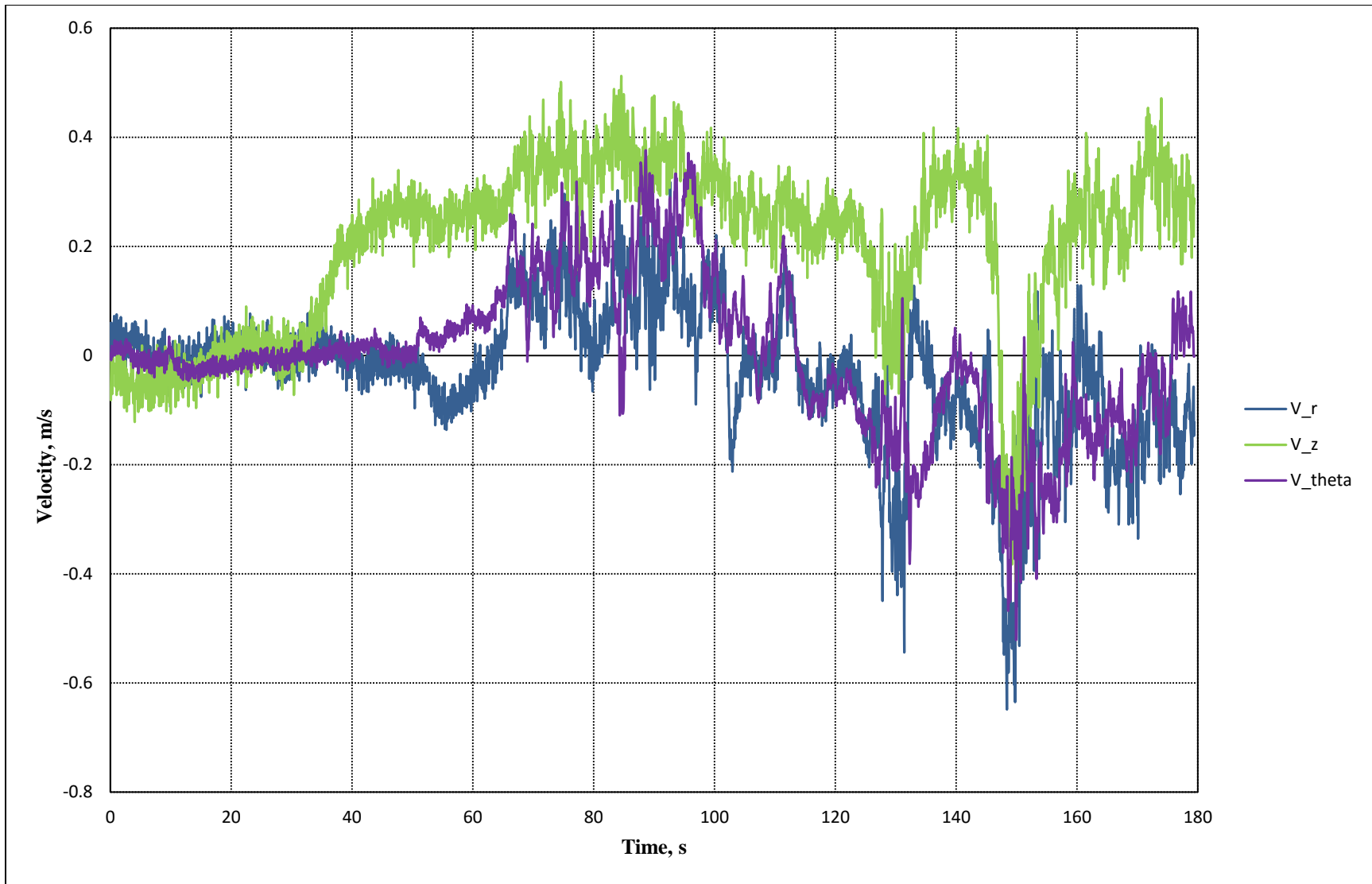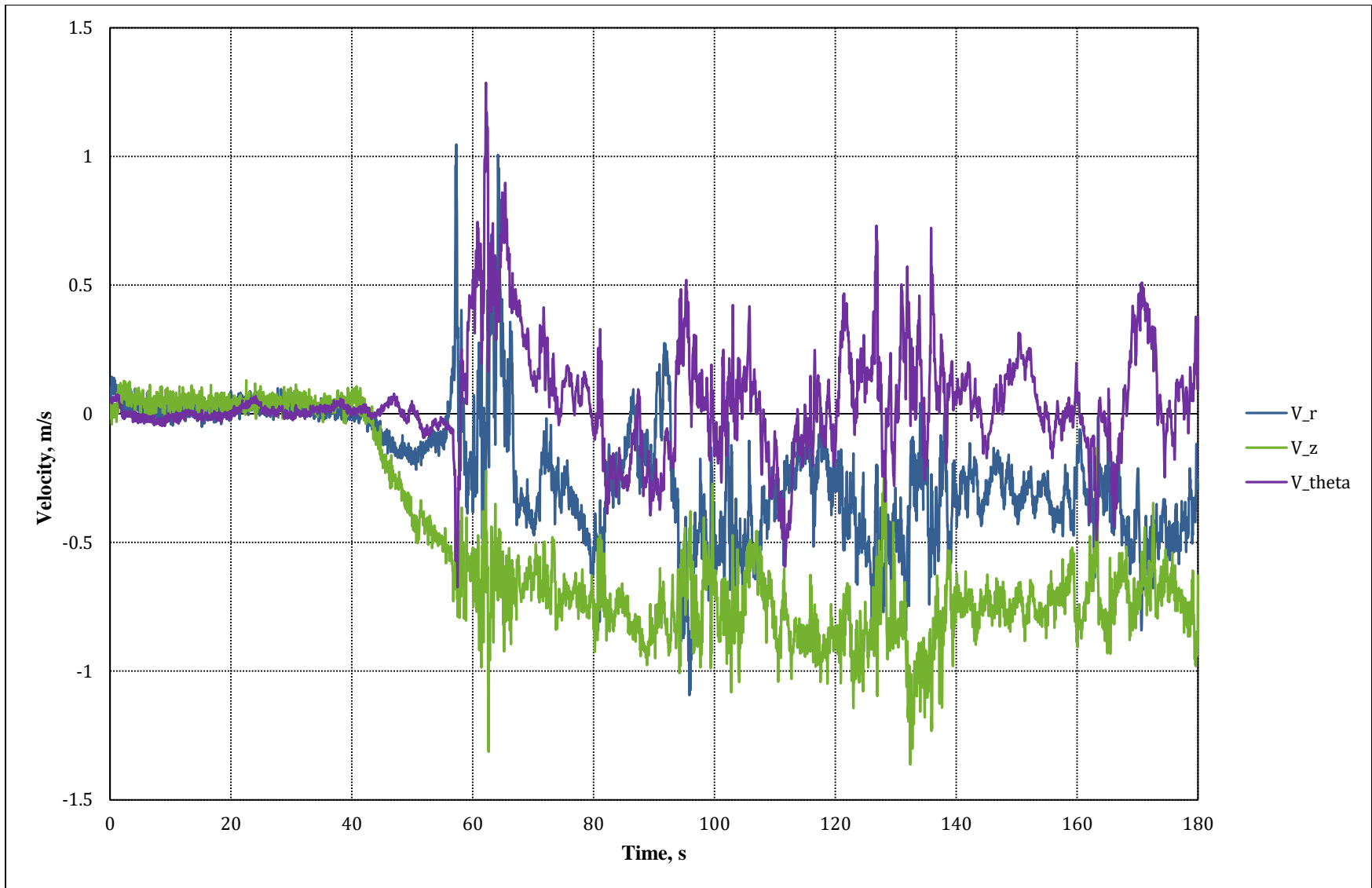
Figure A5. Run2, Point1 velocity data.
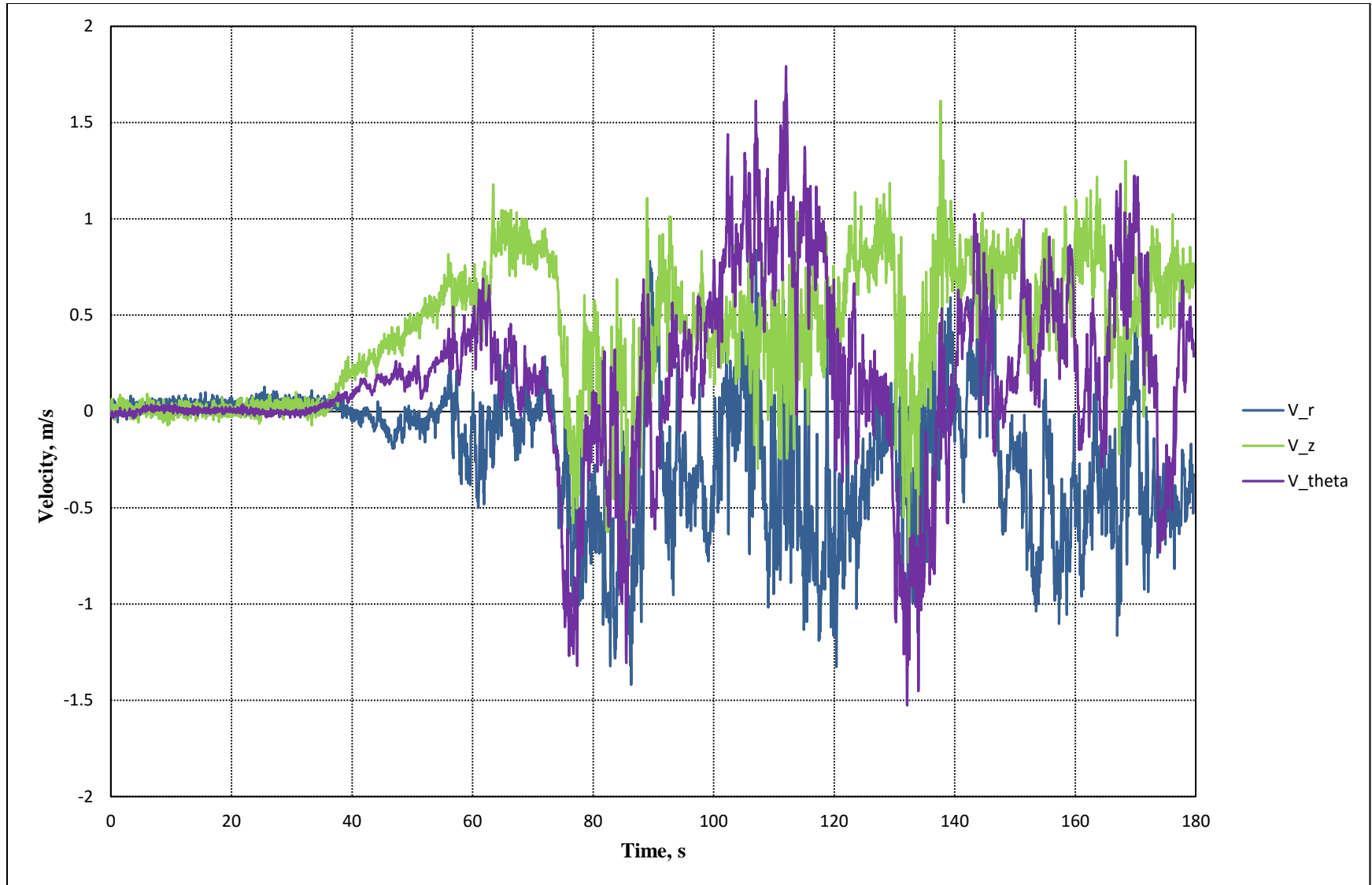
Figure A6. Run2, Point2 velocity data.
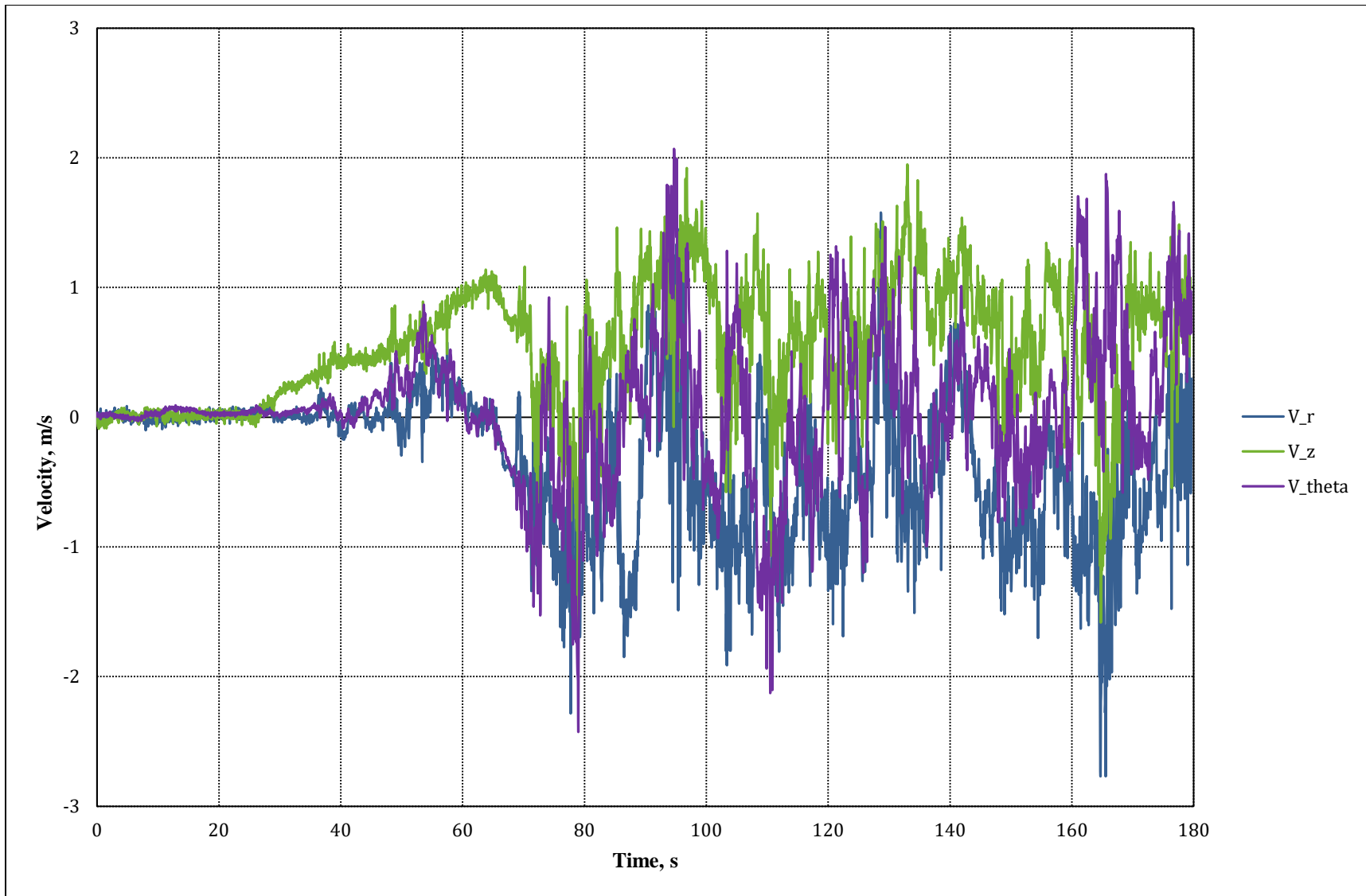
Figure A7. Run2, Point3 velocity data.
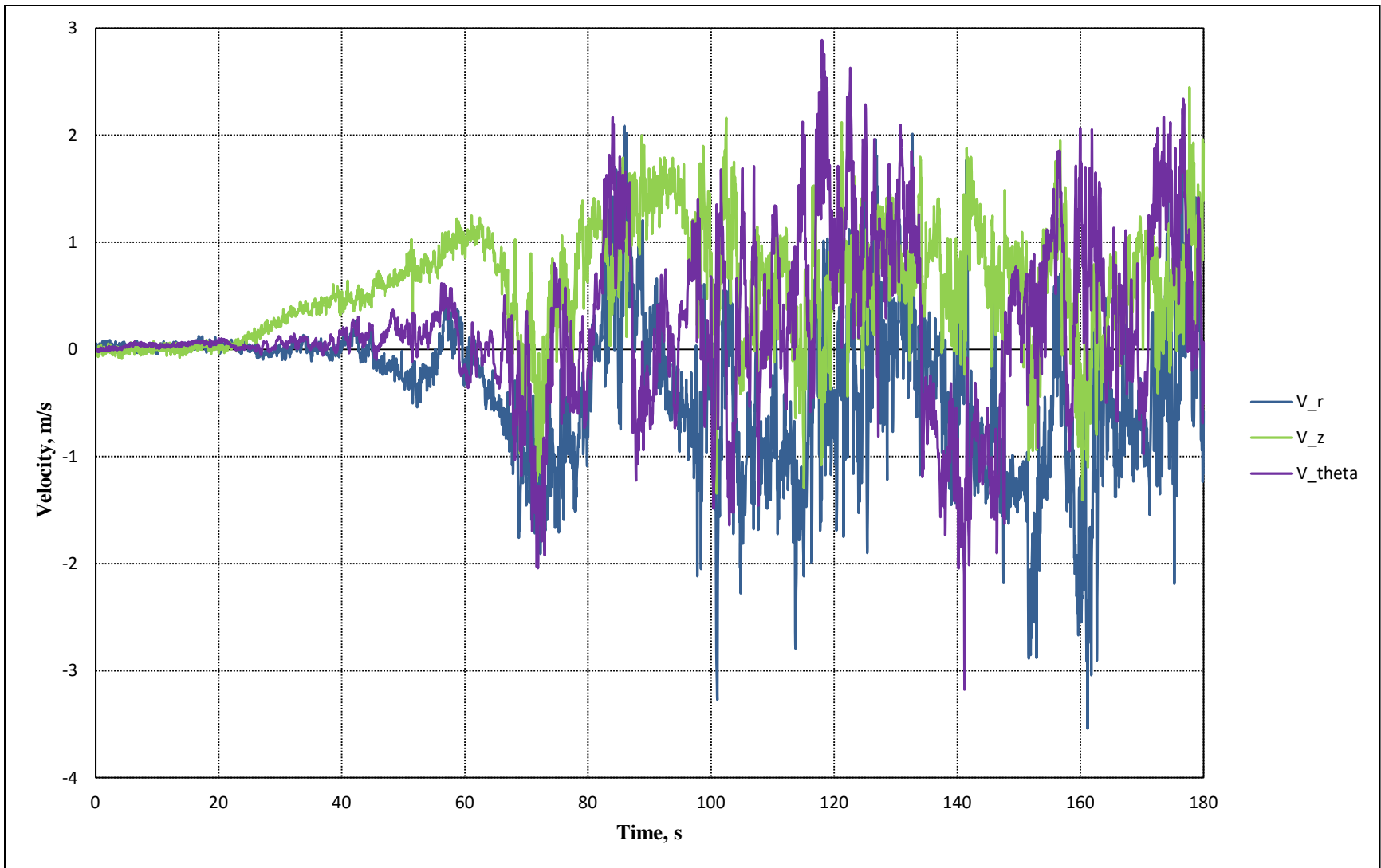
Figure A8. Run2, Point4 velocity data.
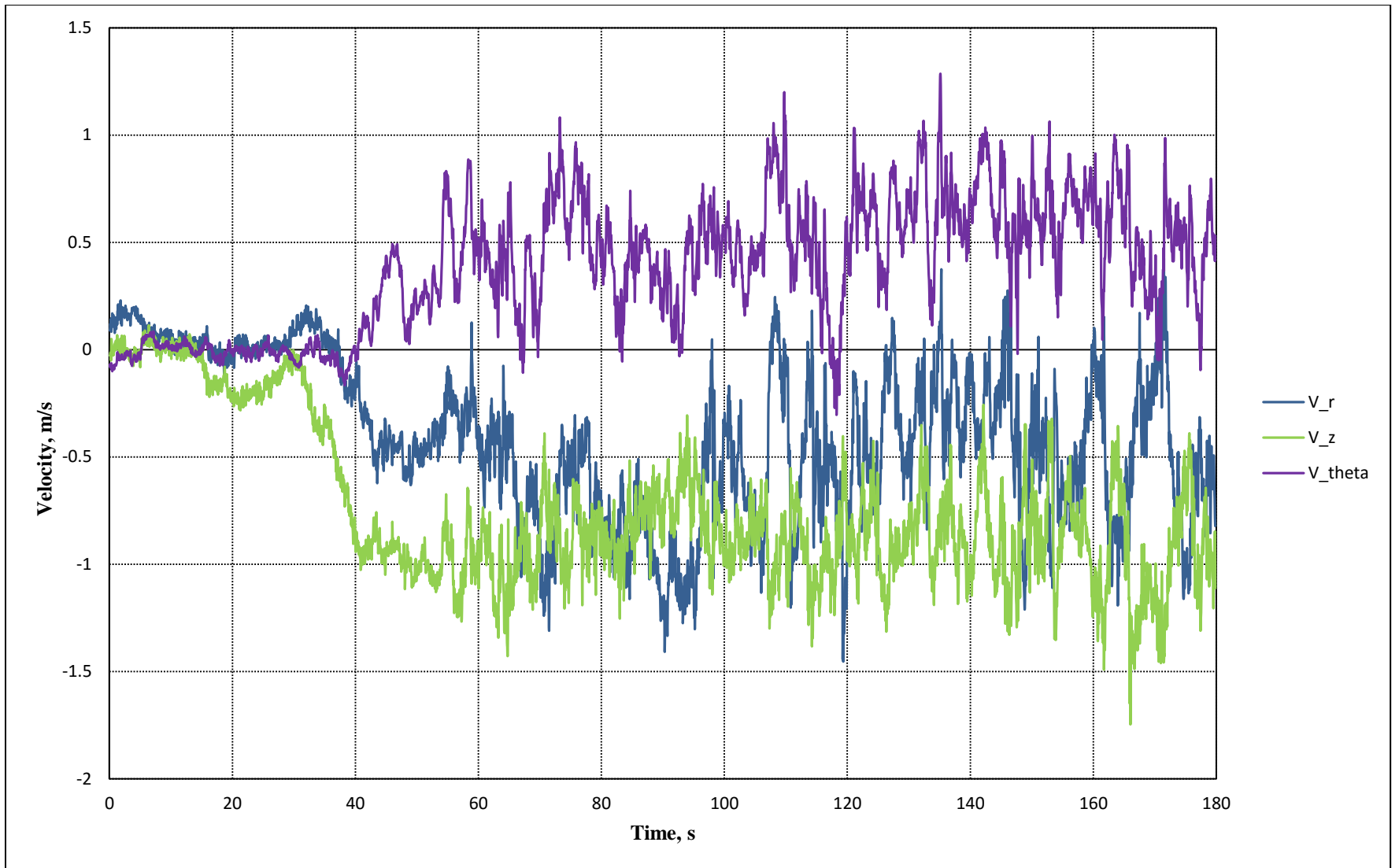
Figure A9. Run3, Point1 velocity data.
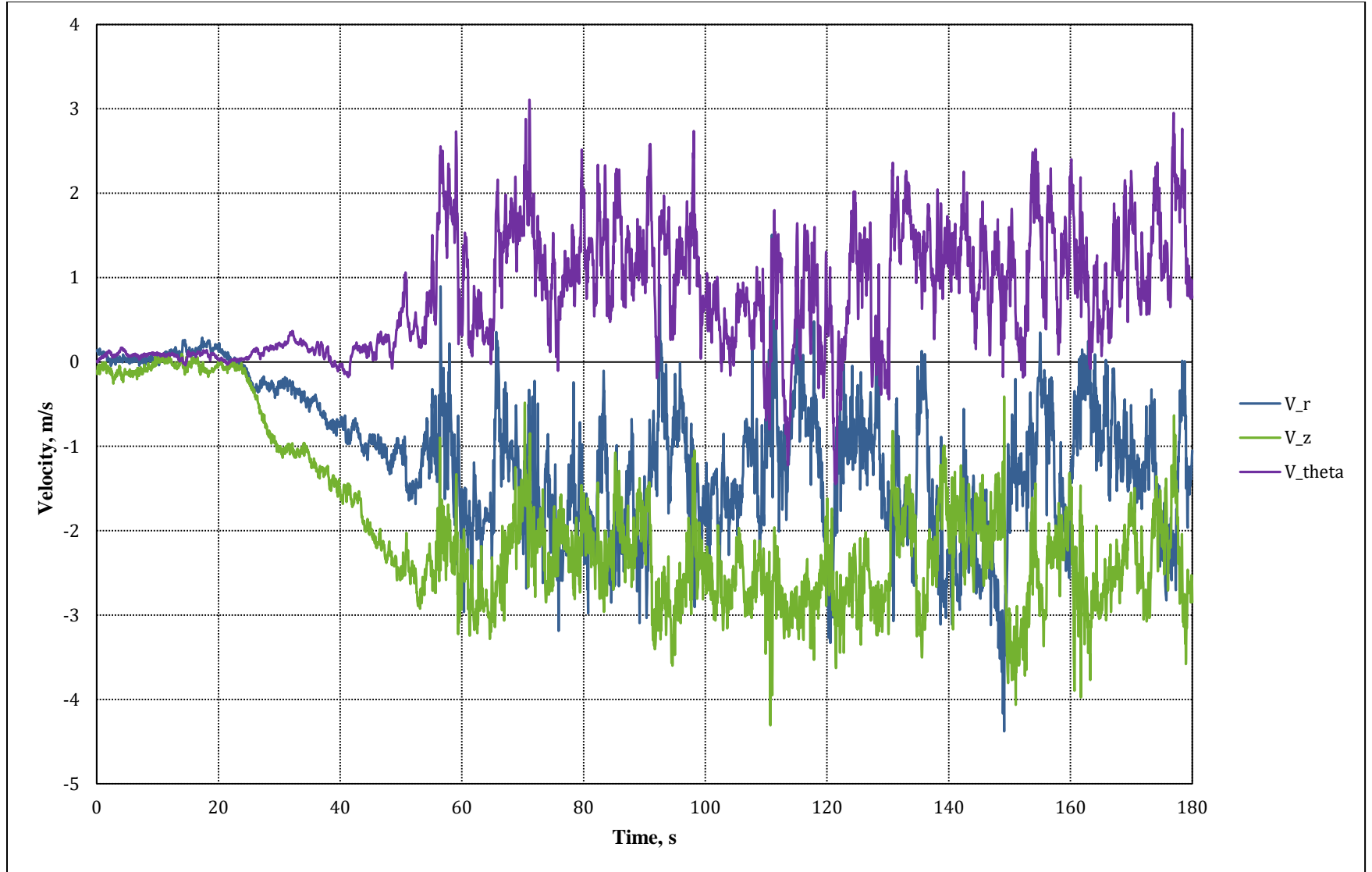
Figure A10. Run3, Point2 velocity data.
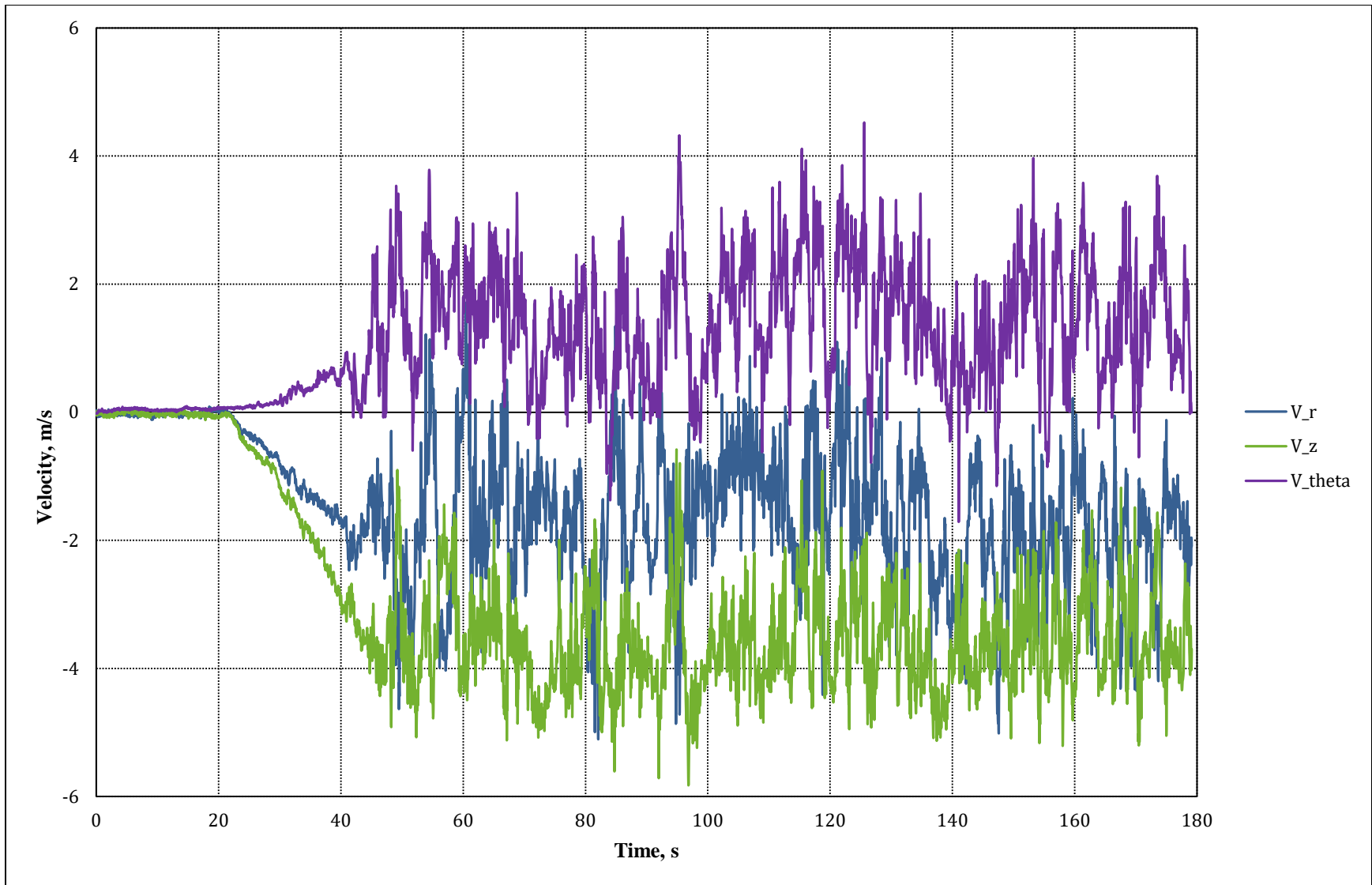
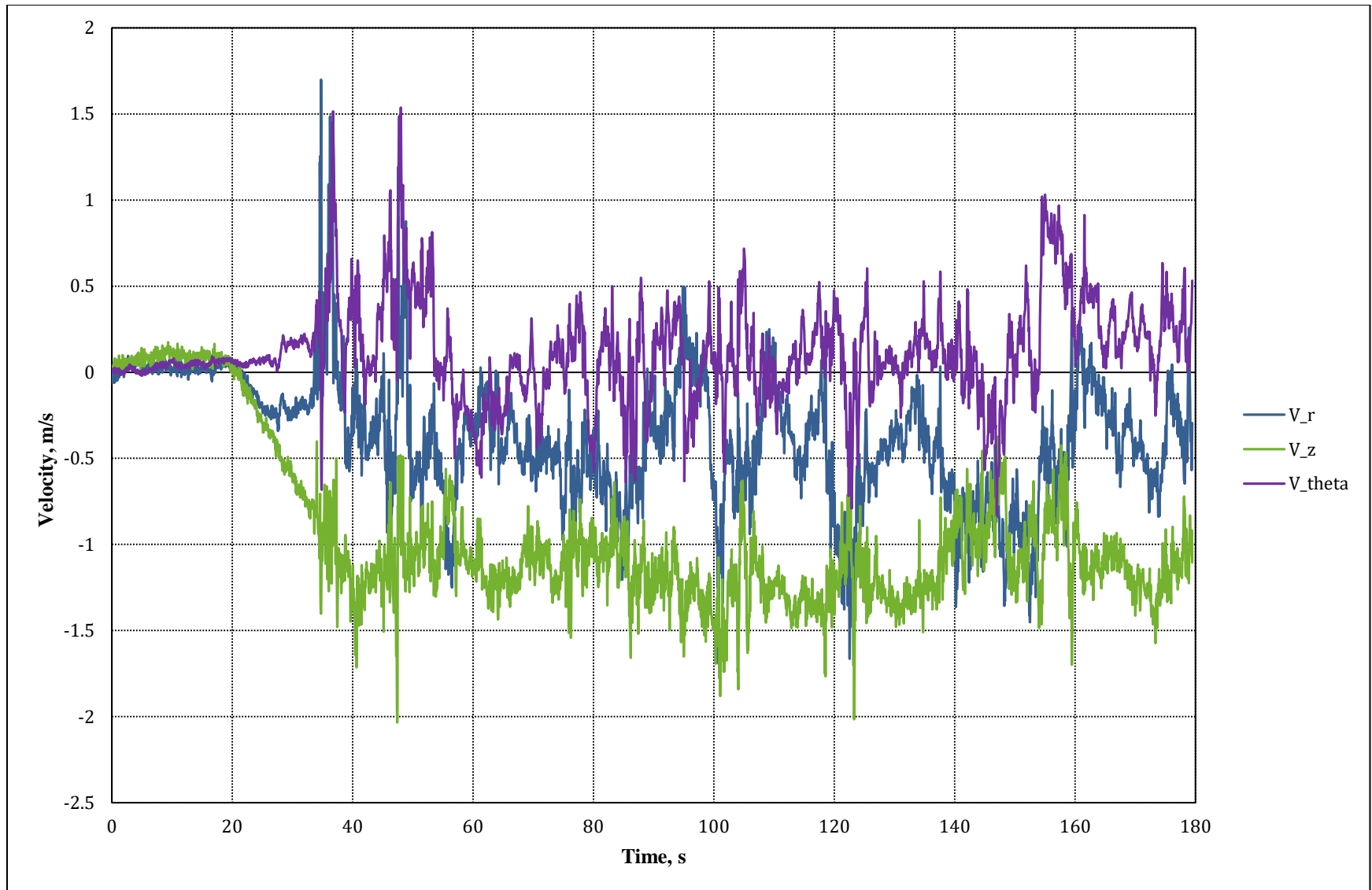Figure A11. Run3, Point3 velocity data.
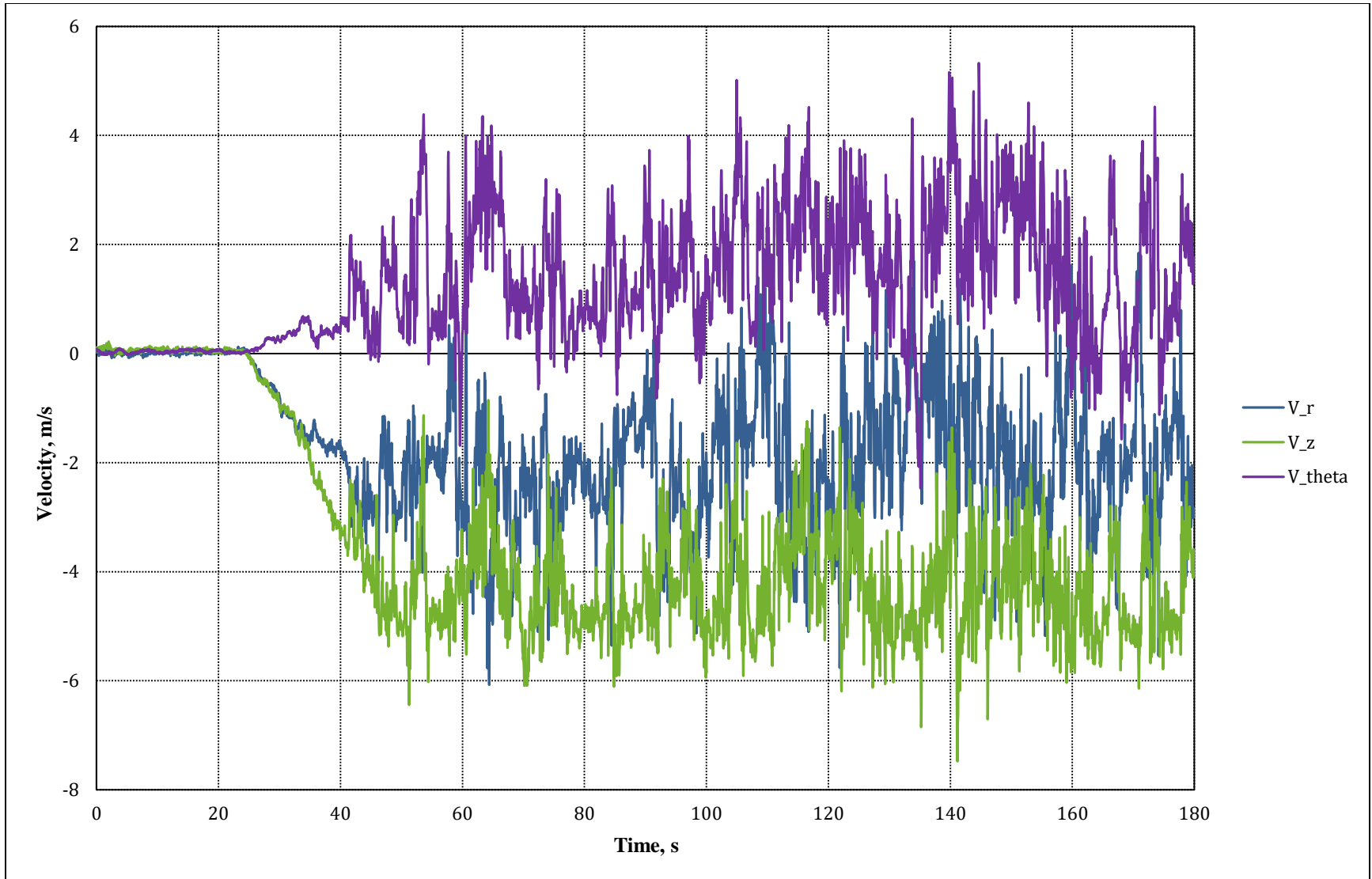
Figure A12. Run3, Point4 velocity data.
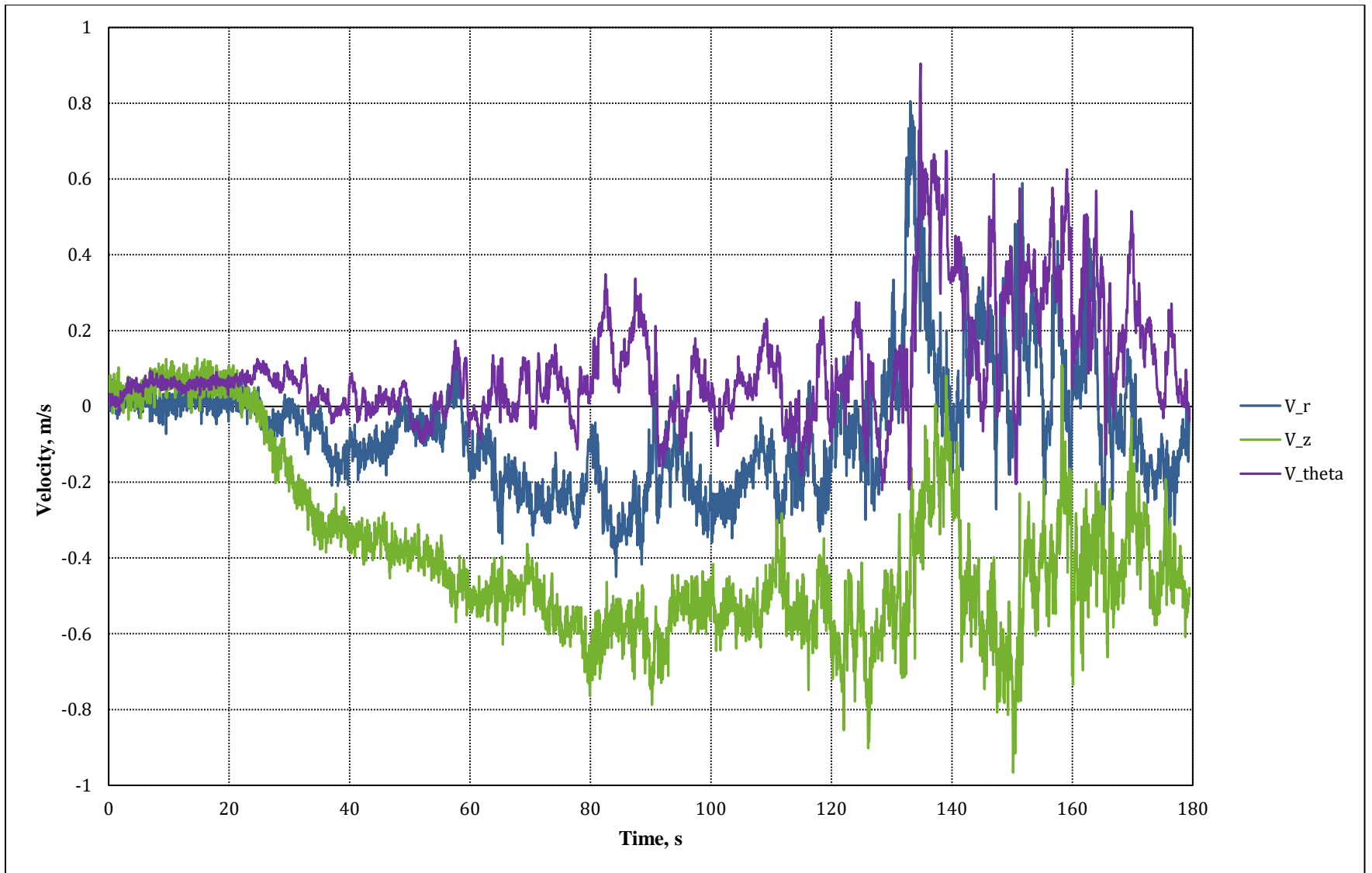
Figure A13. Run4, Point1 velocity data.
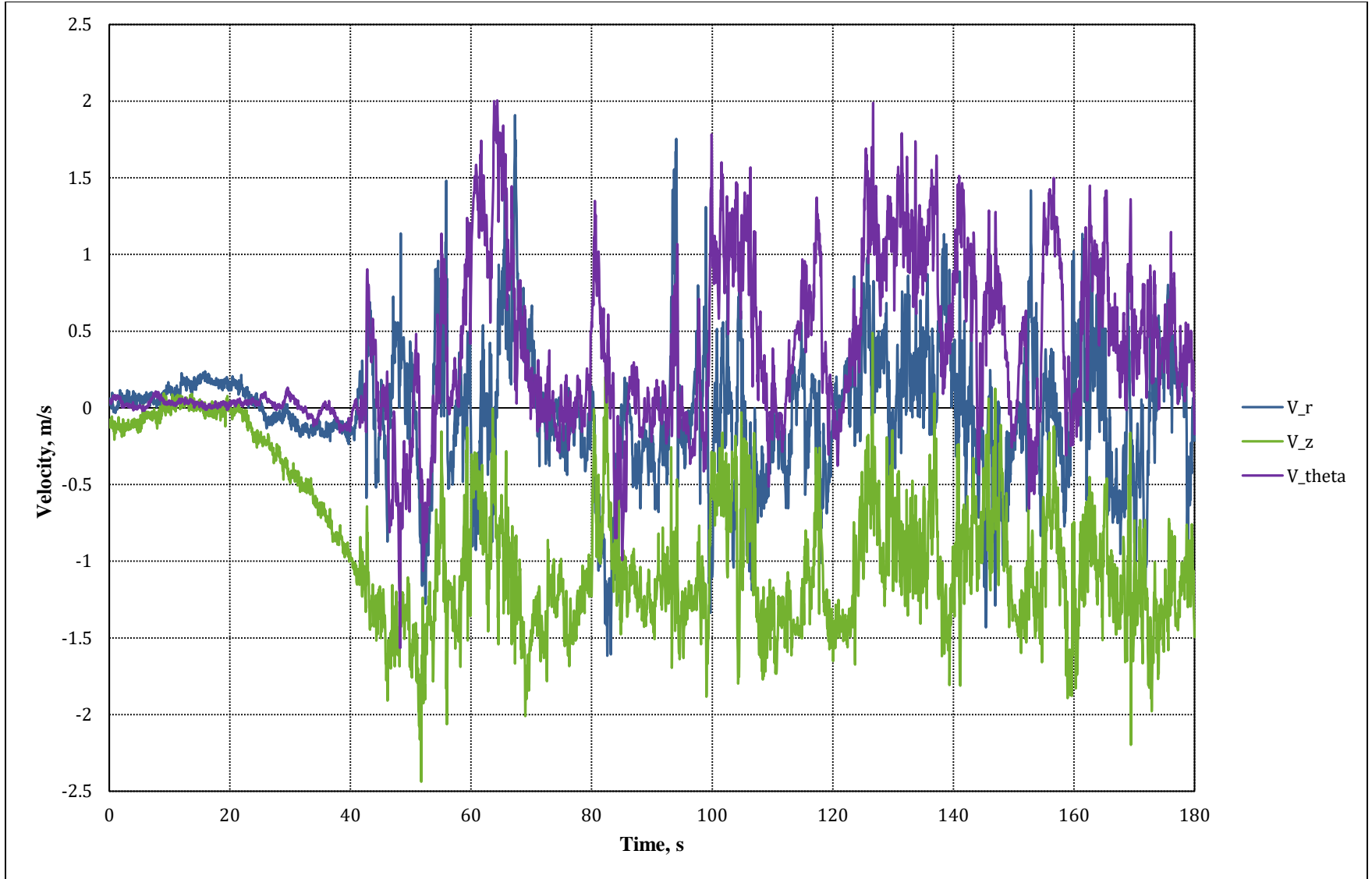
Figure A14. Run4, Point2 velocity data.
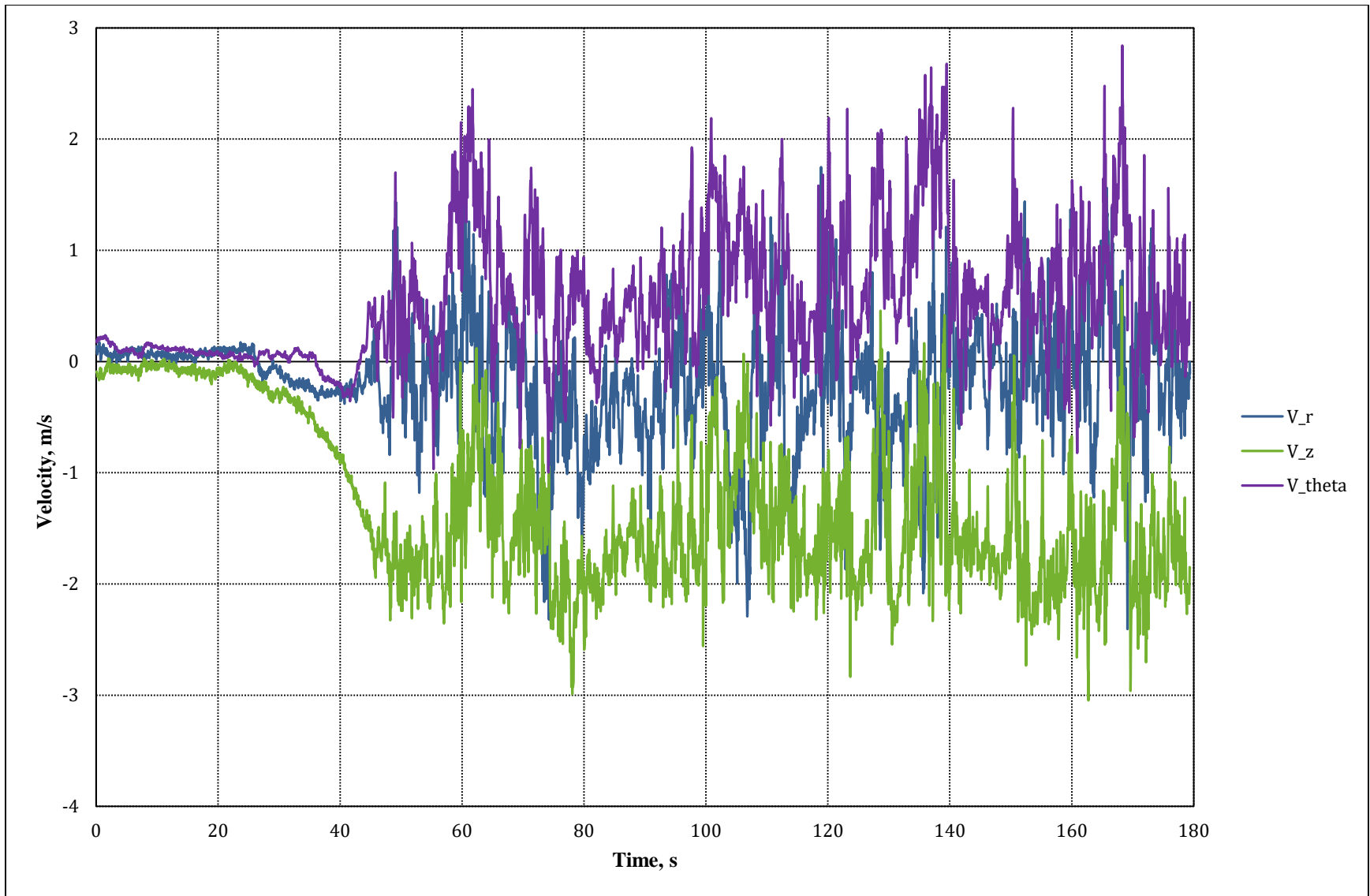
Figure A15. Run4, Point3 velocity data.
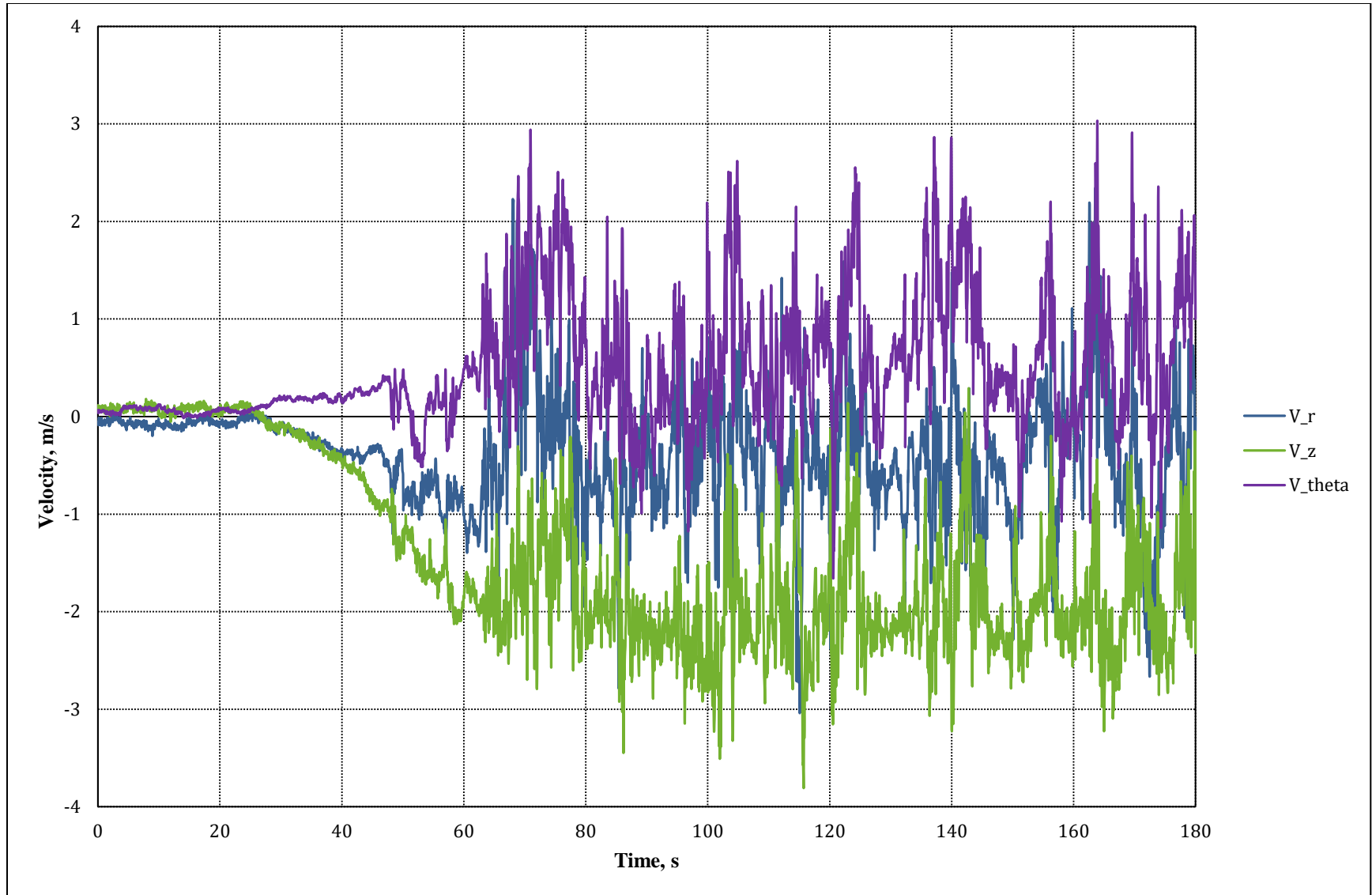
Figure A16. Run4, Point4 velocity data.
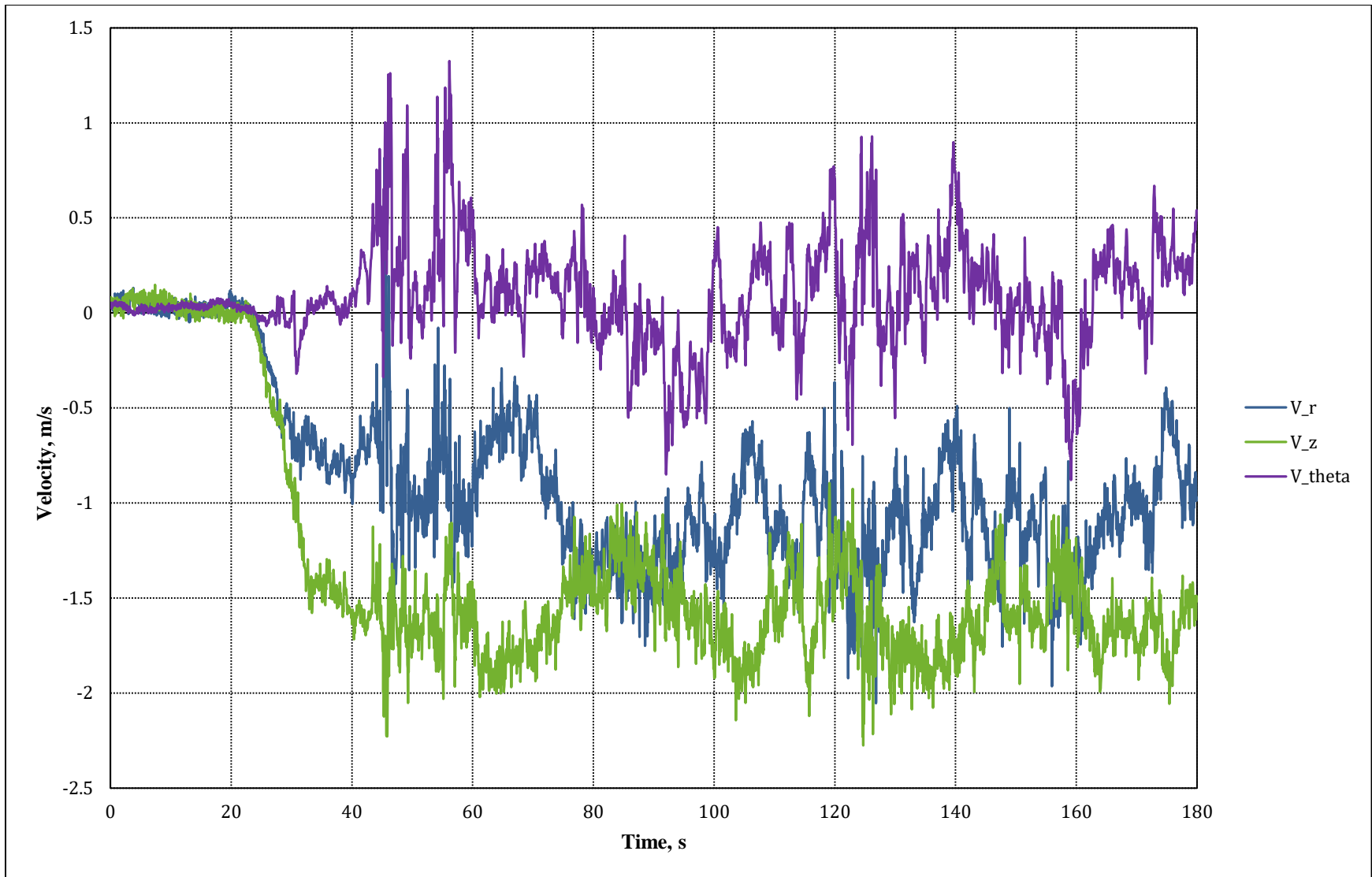
Figure A17. Run5, Point1 velocity data.
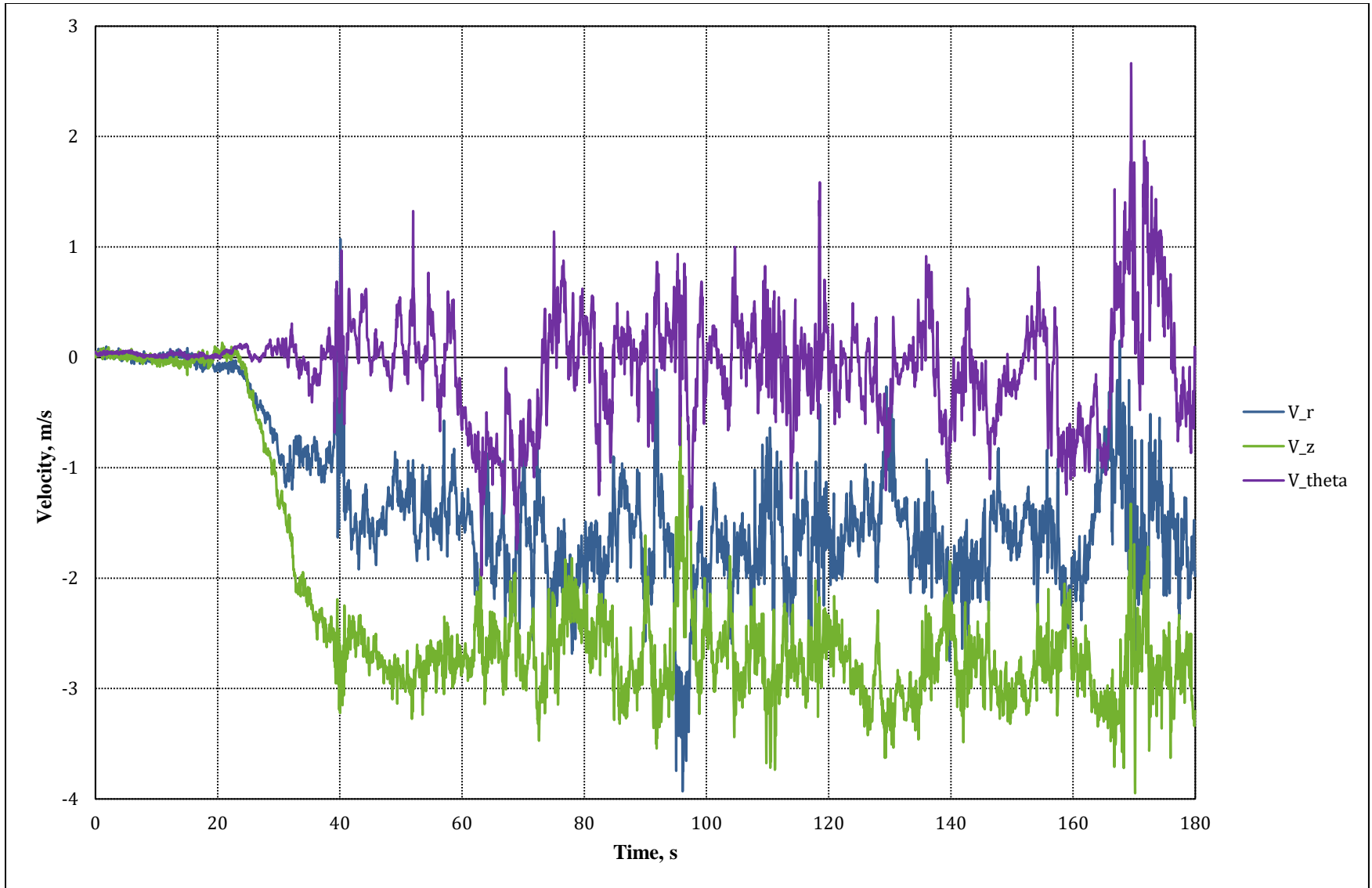
Figure A18. Run5, Point2 velocity data.

Figure A19. Run5, Point3 velocity data.

Figure A20. Run5, Point4 velocity data.

Figure A21. Run6, Point1 velocity data.

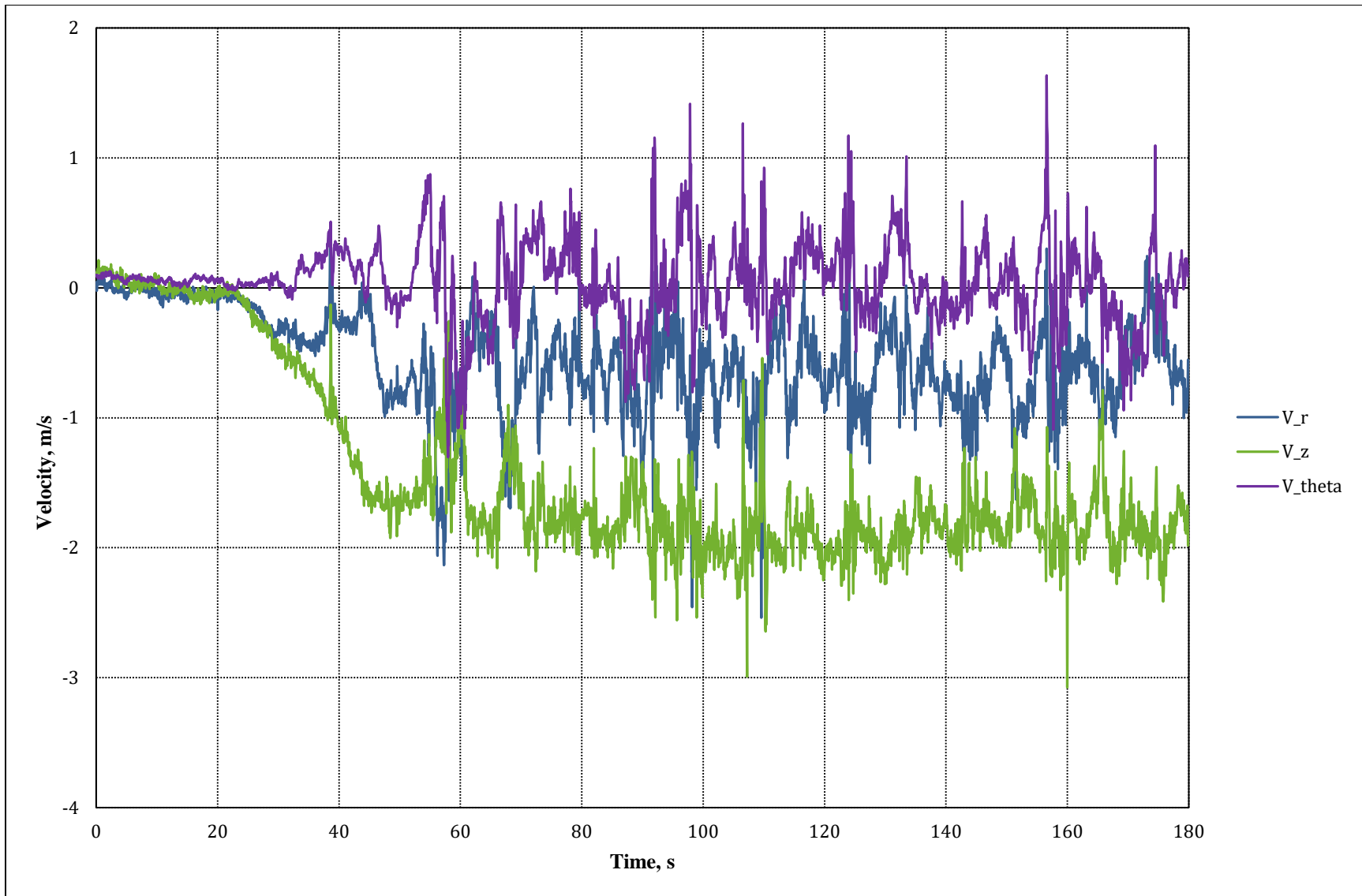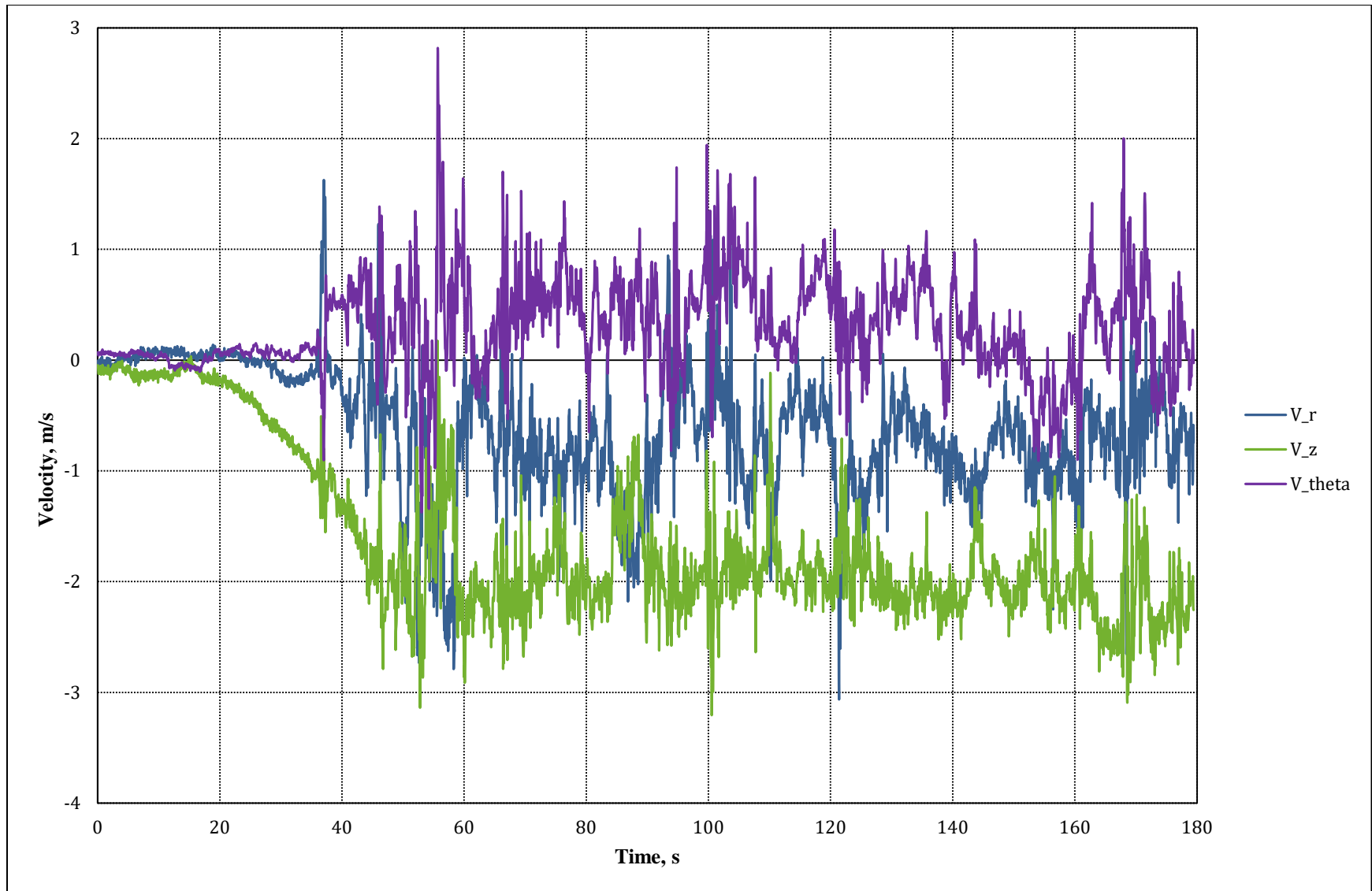Figure A22. Run6, Point2 velocity data.

Figure A23. Run6, Point3 velocity data.

Figure A24. Run6, Point4 velocity data.